

Axion detection via superfluid ^3He ferromagnetic phase and quantum measurement techniques

So Chigusa ^{a,b}, Dan Kondo,^c Hitoshi Murayama ^{a,b,c,1}, Risshin Okabe ^c and Hiroyuki Sudo ^d

^a*Ernest Orlando Lawrence Berkeley National Laboratory, Berkeley, CA 94720, USA*

^b*Department of Physics, University of California, Berkeley, CA 94720, USA*

^c*Kavli Institute for the Physics and Mathematics of the Universe (WPI), University of Tokyo Institutes for Advanced Study, University of Tokyo, Kashiwa 277-8583, Japan*

^d*Institute for Solid State Physics, University of Tokyo, Kashiwa, Chiba 277-8581, Japan*

E-mail: sochigusa@lbl.gov, dan.kondo@ipmu.jp, hitoshi@berkeley.edu, risshin.okabe@ipmu.jp, h.sudo@issp.u-tokyo.ac.jp

ABSTRACT: We propose to use the nuclear spin excitation in the ferromagnetic A_1 phase of the superfluid ^3He for the axion dark matter detection. This approach is striking in that it is sensitive to the axion-nucleon coupling, one of the most important features of the QCD axion introduced to solve the strong CP problem. We review a quantum mechanical description of the nuclear spin excitation and apply it to the estimation of the axion-induced spin excitation rate. We also describe a possible detection method of the spin excitation in detail and show that the combination of the squeezing of the final state with the Josephson parametric amplifier and the homodyne measurement can enhance the sensitivity. It turns out that this approach gives good sensitivity to the axion dark matter with the mass of $\mathcal{O}(1)\mu\text{eV}$ depending on the size of the external magnetic field. We estimate the parameters of experimental setups, e.g., the detector volume and the amplitude of squeezing, required to reach the QCD axion parameter space.

¹Hamamatsu Professor

Contents

1	Introduction	1
2	Understanding ^3He via spinor BEC	3
2.1	Phases of superfluid ^3He	3
2.2	Spinor BEC description of magnetism in the A, A_1 , and A_2 phases	7
2.3	Nuclear magnons in the ferromagnetic A_1 phase	10
3	Axion detection	11
3.1	Axion-magnon conversion	12
3.2	Mixing between magnon and cavity modes	14
3.3	Quantum measurement techniques	15
3.3.1	Squeezing of states	16
3.3.2	Homodyne measurement	18
4	Sensitivity	19
5	Conclusion and Discussion	22
A	Statistical treatment of noise	23
A.1	Formulation	23
A.2	Creation Rate of Magnons	27
A.3	Test Statistic	28
B	Josephson parametric amplifier (JPA)	30
B.1	Effective description	31
B.2	Flux-driven Josephson parametric amplifier	32
B.3	Resonator equation	34

1 Introduction

Axion [1] is a proposed solution to the strong CP problem, namely to explain why the quantum chromodynamics (QCD) does not violate the time-reversal symmetry. The experimental upper limit on the neutron electric dipole moment $d_n < 1.8 \times 10^{-26} e \text{ cm}$ [2] implies that the so-called vacuum angle of QCD to be extremely small $\bar{\theta} < 10^{-10}$. The theory assumes a new global U(1) Peccei–Quinn symmetry broken spontaneously at the energy scale called the axion decay constant f_a as well as explicitly by the QCD anomaly. The effective operator of the axion coupling to gluons is

$$\mathcal{L}_a = \frac{g_s^2}{64\pi^2} \left(\bar{\theta} + \frac{a}{f_a} \right) \epsilon^{\mu\nu\rho\sigma} G_{\mu\nu}^b G_{\rho\sigma}^b . \quad (1.1)$$

Switching to the chiral Lagrangian, it can be shown that the axion settles to the ground state where $\bar{\theta}$ is dynamically canceled.

Interestingly, it was pointed out that the axion can also comprise the dark matter of the Universe from misalignment mechanism or emission from axion strings [3]. The initial version of the theory assumed $f_a = v$ (electroweak scale) and was excluded by beam dump experiments. It was later proposed to take $f_a \gg v$ dubbed “invisible axion” [4–7]. The axion abundance is higher for higher f_a , and $f_a \simeq 10^{12}$ GeV is typically regarded as a preferred range. It translates to $m_a \simeq \mu\text{eV}$ scale.

Many direct detection experiments for the dark matter axion, such as [8–25], rely on the axion coupling to photons $aF_{\mu\nu}\tilde{F}^{\mu\nu}$. Their prospect in the near future is becoming exciting. Yet the axion coupling to photons is highly model-dependent. To fully verify that the axion solves the strong CP problem, measuring its coupling to hadrons would be crucial. In particular, the axion couples to the nucleon spins $\vec{\nabla}a \cdot \vec{s}_N$ with relatively little model dependence. Search for dark matter axion using the nuclear spins, or confirming detected axion signal with nuclear signs, would be crucial to enhance our understanding of both the strong CP problem as well as the nature of dark matter. In spite of its importance, there are relatively few experiments and proposals including [26–37] in this direction.

In this paper, we propose a new experimental technique to detect dark matter axions using their coupling to nuclear spins. Interactions among the nuclear spins are very weak because their magnetic moments are suppressed by the nucleon mass $\mu_N = e/m_N$ rather than the electron mass $\mu_B = e/m_e$. One needs to identify material where nuclear spins play a major role at very low temperatures.

We point out that the A_1 phase of superfluid ^3He is a unique material that has an ordering of nuclear spins without relying on their coupling to electron spins. This is because the Cooper pairs of ^3He atoms are in the p -wave (anti-symmetric) with total spin $S = 1$ (symmetric) as required by Fermi statistics. In a high magnetic field, it becomes basically a ferromagnet of nuclear spins. The corresponding nuclear magnon is gapped due to the external magnetic field and the gap can be tuned to the axion mass. It is quite remarkable that the gap happens to be in the range of the preferred axion mass for dark matter with an achievable magnetic field. Then the magnon can be converted to a cavity photon resonantly due to the polariton mixing between the magnon and photon. Again the size of the cavity is such that it can be fitted in a laboratory. Note that our setup is distinct from other proposals to use superfluid ^3He for axion dark matter search [33, 34] in the superfluid phase used and/or the signal detection method.

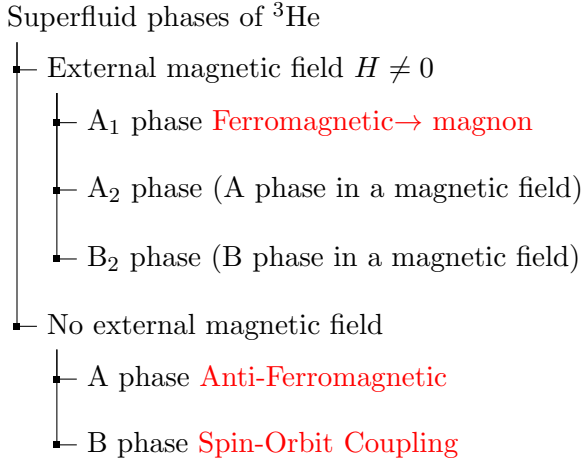
Because our experiments are performed at such low temperatures $T \lesssim 3$ mK that the target ^3He shows superfluidity, the quantum noise [38] becomes non-negligible. These days several applications of quantum measurement techniques to axion detections have been studied in order to circumvent the quantum noise [13, 39–46]. In this paper, we apply the squeezing technique, which has been discussed in [13, 39], and evaluate the improvement in the sensitivity of our experiment.

This paper is organized as follows. In section 2, we review the properties of ^3He . We analyze superfluid phases of ^3He using the spinor BEC formalism and understand the properties of nuclear magnons in the ferromagnetic A_1 phase. In section 3, we discuss

how the axion dark matter signal can be detected using superfluid ^3He ; we use a nuclear magnon mode, which is converted into a cavity photon through the polariton mixing. We also discuss how noise reduction is realized by using squeezing and the homodyne measurement. We show sensitivities for several different setups in section 4 and conclude in section 5. A detailed description of our noise estimate and statistical treatment is summarized in appendix A. Finally, we review the Josephson parametric amplifier (JPA), which is a representative apparatus for squeezing, in appendix B.

2 Understanding ^3He via spinor BEC

In this section, we will describe the phase structure of the superfluid ^3He using Ginzburg-Landau formalism and simplified spinor BEC formalism. We summarize the phase structure in the following tree diagram. The important thing in this paper is that we will use the fact that the A_1 phase has a ferromagnetic property.



In section 2.1, we will sketch the phase structure of ^3He with Ginzburg-Landau formalism. In section 2.2, we will describe the A phase of ^3He with an external magnetic field with spinor BEC formalism. In section 2.3, we will study how to utilize the ferromagnetic property of the A_1 phase of ^3He as magnon.

2.1 Phases of superfluid ^3He

Historically, after the success of the BCS theory [47], people tried to look for the description of the superfluid ^3He because it is liquid and has no lattice structure inside. Some people thought about the pairing states which are not s -wave. One is about the general anisotropic case by Anderson and Morel [48]. This model has a peculiar feature that the nodes exist on the Fermi surface for the axial p -wave state (ABM state named after Anderson-Brinkman-Morel). It turned out that this theory describes what is called the A phase nowadays. The number of the substates for p -wave Cooper pair is three. Later, it was shown that the mixing of all these states is favored energetically [49], which turned out to be the B phase nowadays. At early stages, the thermodynamic properties are explored by Leggett using the framework of renormalized quasi-particles [50, 51]. Experimentally, the A and B phases

were discovered at 2.6 mK and 1.8 mK respectively [52], which confirmed the existence of the phase structure of the superfluid ^3He .

The nucleus of a ^3He atom consists of two protons and one neutron. The proton spins are aligned anti-parallel with each other, while the neutron spin is isolated, making the total spin angular momentum to be $I = 1/2$. In the superfluid phase, two ^3He atoms form a Cooper pair, whose ground state is a spin-triplet p -wave condensate [53]. The corresponding order parameter is expressed in terms of annihilation operators of nuclei $\hat{a}_{\vec{k}\alpha}$ as

$$\langle \hat{a}_{-\vec{k}\beta} \hat{a}_{\vec{k}\alpha} \rangle \propto \Delta_{\vec{k}\alpha\beta} \equiv \sum_{\mu=1}^3 d_{\mu}(\vec{k}) (\sigma_{\mu} i \sigma_2)_{\alpha\beta}, \quad (2.1)$$

where \vec{k} and α (β) are the momentum and the spin of a ^3He nucleus, respectively, and σ_{μ} is the Pauli matrix. Since a Cooper pair forms a spin-triplet $L = 1$ relative angular momentum state, the vector $d_{\mu}(\vec{k})$ can be represented as a linear combination of spherical harmonics $Y_{1m}(\vec{k}/|\vec{k}|) \propto \vec{k}/|\vec{k}|$,

$$d_{\mu}(\vec{k}) = \sqrt{3} \sum_{j=1}^3 A_{\mu j} \frac{\vec{k}_j}{|\vec{k}_j|}. \quad (2.2)$$

The phenomenological Lagrangian of the Cooper pairs, i.e., Ginzburg–Landau Lagrangian, can be expressed in terms of the 3×3 order parameter matrix $A_{\mu j}$ [54, 55]. The index $\mu = 1, 2, 3$ refers to the $S = 1$ states while $j = 1, 2, 3$ to the $L = 1$ state both in the Cartesian basis. Namely $A_{\mu j}$ transforms as a bi-vector under $\text{SO}(3)_L \times \text{SO}(3)_S$. Note that $A_{\mu j}$ is complex as its phase $\text{U}(1)_{\phi}$ corresponds to the conserved number operator of the Cooper pairs. Because the Lagrangian has to be Hermitian and invariant under the global $\text{SO}(3)_L \times \text{SO}(3)_S \times \text{U}(1)_{\phi}$ symmetry, we have only one second-order term of $A_{\mu j}$

$$I_0 = \text{tr}(AA^{\dagger}), \quad (2.3)$$

and five fourth-order terms

$$I_1 = |\text{tr}(AA^T)|^2, \quad (2.4)$$

$$I_2 = \left[\text{tr}(AA^{\dagger}) \right]^2, \quad (2.5)$$

$$I_3 = \text{tr}[(AA^T)(AA^T)^*], \quad (2.6)$$

$$I_4 = \text{tr}[(AA^{\dagger})^2], \quad (2.7)$$

$$I_5 = \text{tr}[(AA^{\dagger})(AA^{\dagger})^*], \quad (2.8)$$

in the effective potential. As a result, in the absence of any external fields, the effective potential per volume is given by

$$V_0 = \alpha(T)I_0 + \frac{1}{2} \sum_{i=1}^5 \beta_i I_i, \quad (2.9)$$

where we neglect higher-order terms of $A_{\mu j}$, which can be justified when we consider the phenomenology of a system sufficiently close to the phase transition, and the numerical values of $|A_{\mu j}|$ are small. The coefficients α and β_i are determined by the microscopic theory. For example, they have been calculated in the weak-coupling theory [53], and their numerical values are

$$\alpha(T) \sim -10^{-3} \left(1 - \frac{T}{T_c}\right) \mu\text{eV}^{-1} \text{\AA}^{-3}, \quad (2.10)$$

$$(\beta_1^{\text{WC}}, \beta_2^{\text{WC}}, \beta_3^{\text{WC}}, \beta_4^{\text{WC}}, \beta_5^{\text{WC}}) = \frac{6}{5} \beta_0 \left(-\frac{1}{2}, 1, 1, 1, -1\right), \quad (2.11)$$

$$\beta_0 \sim 10^{-3} \mu\text{eV}^{-3} \text{\AA}^{-3}, \quad (2.12)$$

where T_c is the transition temperature ~ 2.6 mK in the absence of external magnetic fields. The values of β_i can differ from those of β_i^{WC} depending on pressure. Nevertheless, we will use the numerical values in eqs. (2.11) and (2.12) for β_i below since the experimentally measured values differ from β_i^{WC} by only $\mathcal{O}(1)$ factors, $(\beta_i - \beta_i^{\text{WC}})/\beta_0 \simeq \mathcal{O}(1)$ [56].

As noted above, the effective Lagrangian has a global symmetry $\text{SO}(3)_L \times \text{SO}(3)_S \times \text{U}(1)_\phi$, which corresponds to the rotation in the momentum space, the rotation in the spin space, and the overall phase rotation, respectively. It is known that, depending on the values of coefficients in eq. (2.9), the matrix A acquires a non-zero expectation value in the ground state, which spontaneously breaks the global symmetry and leads to different phases. Without an external magnetic field, there are two superfluid phases for ${}^3\text{He}$, the A and B phases. Their expectation values are expressed as

$$\text{A phase: } A_{\mu j} \propto \frac{1}{\sqrt{2}} \begin{pmatrix} 0 & 0 & 0 \\ 0 & 0 & 0 \\ 1 & i & 0 \end{pmatrix}, \quad (2.13)$$

$$\text{B phase: } A_{\mu j} \propto \frac{1}{\sqrt{3}} e^{i\phi} R_{\mu j}(\vec{n}, \theta), \quad (2.14)$$

where ϕ is an overall phase, and $R_{\mu j}$ is a relative rotation of the spin and orbital spaces, represented by a rotation axis \vec{n} and a rotation angle θ . Note that there are more than one choice of the order parameter in the A phase corresponding to the choices of particular directions of spin and orbital spaces, both of which are assumed to be the z -axis in the above expression.

When we turn on an external magnetic field \vec{B} , the potential V has two more invariant terms

$$F^{(1)} = i\eta \sum_{\mu\nu\lambda j} \epsilon_{\mu\nu\lambda} B_\mu A_{\nu j}^* A_{\lambda j}, \quad (2.15)$$

$$F^{(2)} \propto \sum_{\mu\nu j} B_\mu A_{\mu j} B_\nu A_{\nu j}^*. \quad (2.16)$$

The term $F^{(1)}$ is there only for the indices μ, ν because the ${}^3\text{He}$ atoms are electrical neutral and their orbital angular momentum does not have a magnetic moment, while their spins

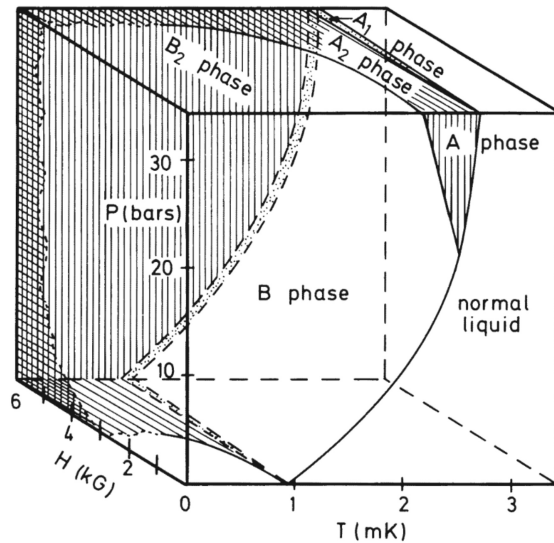


Figure 1. The phase diagram of the superfluid ${}^3\text{He}$ taken from [53].

do. Assuming that \vec{B} is along the z -direction, one can see that $F^{(1)}$ and $F^{(2)}$ break the global symmetry to $\text{SO}(3)_L \times \text{U}(1)_{S_z} \times \text{U}(1)_\phi$. Because these interaction terms $F^{(1)}$ and $F^{(2)}$ bring three types of spontaneous symmetry breaking depending on the coefficients, there are three corresponding phases:

$$\text{A}_1 \text{ phase: } A_{\mu j} \propto \frac{1}{2} \begin{pmatrix} 1 & i & 0 \\ i & -1 & 0 \\ 0 & 0 & 0 \end{pmatrix}, \quad (2.17)$$

$$\text{A}_2 \text{ phase: } A_{\mu j} \propto \frac{1}{\sqrt{2(|p_1|^2 + |p_2|^2)}} \begin{pmatrix} p_1 & ip_1 & 0 \\ ip_2 & -p_2 & 0 \\ 0 & 0 & 0 \end{pmatrix}, \quad (2.18)$$

$$\text{B}_1 \text{ phase: } A_{\mu j} \propto \frac{e^{i\phi}}{\sqrt{2[2(|p_1|^2 + |p_2|^2) + |p_3|^2]}} \begin{pmatrix} p_1 & p_2 & 0 \\ \pm p_2 & \mp p_1 & 0 \\ 0 & 0 & p_3 \end{pmatrix}, \quad (2.19)$$

where the real parameters p_1 , p_2 , and p_3 are uniquely determined as functions of the coefficients $\alpha(T)$ and β_i , as demonstrated in the next section.

In fig. 1, we show the phase diagram of the superfluid ${}^3\text{He}$ as a function of the temperature T , the pressure P , and the external magnetic field H taken from [53]. We can see from the figure that the A_1 phase of our interest can be realized by carefully setting pressure P , temperature T , and the external magnetic field H ; for example, $P \sim \mathcal{O}(1)$ bars, $T \sim \mathcal{O}(1)$ mK, and $H \gtrsim \mathcal{O}(1)$ T. In the next subsection, we will see in more detail the criteria for which phase is realized, focusing on the A, A_1 , and A_2 phases.

2.2 Spinor BEC description of magnetism in the A, A₁, and A₂ phases

Hereafter, we focus on the A, A₁, and A₂ phases, which have a unified description with the so-called spinor BEC formalism by keeping only the spin degree of freedom. The spinor BEC refers to a Bose–Einstein condensate of atoms with integer spin, see e.g., for a review [57, 58]. This procedure is appropriate partly because the unbroken symmetries of these phases do not mix the rotations in spin and orbital spaces unlike the B phases. Thus, if we do not consider excitation of the orbital angular momentum of ³He, we can focus only on the spin space. For this purpose, we define a *spinor* order parameter \vec{c} by fixing $L_z = +1$ as

$$A_{\mu j} = \frac{1}{\sqrt{2}}(\vec{c}, i\vec{c}, 0). \quad (2.20)$$

We can rewrite invariant terms I_i and $F^{(1)}$ in terms of \vec{c} as

$$I_0 = \vec{c}^* \cdot \vec{c}, \quad (2.21)$$

$$I_2 = (\vec{c}^* \cdot \vec{c})^2, \quad (2.22)$$

$$I_4 = (\vec{c}^* \cdot \vec{c})^2, \quad (2.23)$$

$$I_5 = |\vec{c} \cdot \vec{c}|^2 = [(\vec{c}^* \times \vec{c})^2 + (\vec{c}^* \cdot \vec{c})^2], \quad (2.24)$$

$$F^{(1)} = i\eta\vec{B} \cdot (\vec{c}^* \times \vec{c}). \quad (2.25)$$

Here, we do not consider the invariants I_1 , I_3 , and $F^{(2)}$ because these terms vanish for the A₁ and A₂ phases. Finally, we get a simplified effective potential with the external magnetic field

$$V = \alpha(T)(\vec{c}^* \cdot \vec{c}) + \frac{\beta_{245}}{2}(\vec{c}^* \cdot \vec{c})^2 + \frac{\beta_5}{2}(\vec{c}^* \times \vec{c})^2 + i\eta\vec{B} \cdot (\vec{c}^* \times \vec{c}). \quad (2.26)$$

Here, we have defined a new parameter,

$$\beta_{245} \equiv \beta_2 + \beta_4 + \beta_5. \quad (2.27)$$

Note that $\beta_{245} > 0$ and $\beta_5 < 0$ according to eq. (2.11). In the following, we discuss the magnetism of the A₁ and A₂ phases with this potential.

Using the simplified effective potential, we can easily analyze the potential form as a function of parameters.¹ In the absence of an external magnetic field, only the temperature plays an important role. For $T > T_c$, since $\alpha(T) > 0$ according to eq. (2.10), the potential V has a global minimum at $\vec{c} = \vec{0}$, while for $T < T_c$ or $\alpha(T) < 0$, there is a global minimum at $\vec{c} \propto (0, 0, 1)^T$ with the potential energy $-\alpha^2/(2\beta_{245}) < 0$. The former corresponds to the normal liquid phase, while the latter is consistent with the matrix structure of the A-phase order parameter (2.13).

¹Note that there can be a deeper minimum of the potential, which cannot be described by the spinor BEC formalism. Such a phase may correspond to the B or B₁ phase due to the spin-orbit couplings which originate from a long-distance dipole-dipole interaction among magnetic moments. However this effect is small and can be ignored in the presence of a strong magnetic field. It is worth noting, however, that any of the A, A₁, and A₂ phases can be a global minimum of V for reasonable choices of temperature, external magnetic field, and pressure, such as $T \simeq T_c$ and $B_z \sim \mathcal{O}(1)$ T under the standard atmosphere.

Next, we turn on the external magnetic field $\vec{B} = (0, 0, B_z)^T$ with $\eta B_z > 0$. Restricting the form of \vec{c} to be $(p_1, ip_2, 0)^T$ with $p_1, p_2 \in \mathbb{R}$, we obtain local minima of V expressed as

$$V = 0 \quad \text{at} \quad \vec{c} = \vec{0}, \quad (2.28)$$

$$V = V_1 \equiv -\frac{\alpha(T)^2 (x+y)^2}{2\beta_{245} y(1+y)} \quad \text{at} \quad \vec{c} = \vec{c}_1 \equiv \sqrt{\frac{-\alpha(T)(x+y)}{2\beta_{245}(1+y)}} \begin{pmatrix} 1 \\ i \\ 0 \end{pmatrix}, \quad (2.29)$$

$$V = V_2 \equiv -\frac{\alpha(T)^2 x^2 + y}{2\beta_{245} y} \quad \text{at} \quad \vec{c} = \vec{c}_2 \equiv \sqrt{\frac{-\alpha(T)}{2\beta_{245}}} \begin{pmatrix} \sqrt{1 + \sqrt{1-x^2}} \\ i\sqrt{1 - \sqrt{1-x^2}} \\ 0 \end{pmatrix}, \quad (2.30)$$

where we defined dimensionless variables

$$x \equiv \frac{\beta_{245}\eta B_z}{\alpha(T)\beta_5} \propto B_z \left(1 - \frac{T}{T_c}\right)^{-1}, \quad (2.31)$$

$$y \equiv -\frac{\beta_{245}}{\beta_5} > 0. \quad (2.32)$$

The value of x determines which of the local minima is the global minimum of V as shown in fig. 2. Note that for $p_1 \in \mathbb{R}$, the local minimum $\vec{c} = \vec{c}_1$ exists only when $x < -y$ or $x > 0$. Similarly, the local minimum $\vec{c} = \vec{c}_2$ exists when $0 < x < 1$. When $0 < x < 1$, we have $V_1 \geq V_2$, and this region corresponds to the A_2 phase (the blue region of fig. 2). When $x > 1$ or $x < -y$, we have $V_2 \geq V_1$, which corresponds to the A_1 phase (the red region). When $-y < x < 0$, we obtain the normal liquid phase (the gray region).

For later convenience, we define a normalized order parameter

$$\vec{\phi} \equiv \frac{\sqrt{n}}{\Delta} \vec{c}, \quad (2.33)$$

where Δ is a normalization factor with a dimension of energy defined as

$$\Delta \equiv \sqrt{\vec{c}^* \cdot \vec{c}}, \quad (2.34)$$

so that $\vec{\phi}^* \cdot \vec{\phi} = n$ with n being the number density of Cooper pairs. Given that the typical interatomic spacing is $\sim 3.5 \text{ \AA}$ in the superfluid ^3He , we can estimate $2n \simeq 0.023 \text{ \AA}^{-3}$. This is obtained by two independent ways [59] that agree with each other; one is to use the Green function Monte-Carlo method to solve the many-body Schrödinger equation to calculate ground state properties [60, 61], while the other is the variational method, which is constructed by the Slator determinant for the correlation pairs [62, 63]. The effective potential is now given by

$$V = -\mu \vec{\phi}^* \cdot \vec{\phi} + \frac{\mu}{2v^2} (\vec{\phi}^* \cdot \vec{\phi})^2 - \lambda (\vec{\phi}^* \times \vec{\phi})^2 + ig\mu_N \vec{B} \cdot (\vec{\phi}^* \times \vec{\phi}), \quad (2.35)$$

with some new parameters $\mu \equiv -\alpha(T)F$, $v^2 \equiv -\alpha(T)/(\beta_{245}F)$, $\lambda \equiv -\beta_5 F^2/2$, and $g\mu_N \equiv \eta F$ with $F \equiv \Delta^2/n$. Typical sizes of parameters are estimated as $\mu \sim \text{neV}$, $v \sim \text{\AA}^{-3/2}$, and $\lambda \sim \text{neV}\text{\AA}^3$. In the last term of the potential, $g \simeq -4.3$ is the g -factor of the ^3He

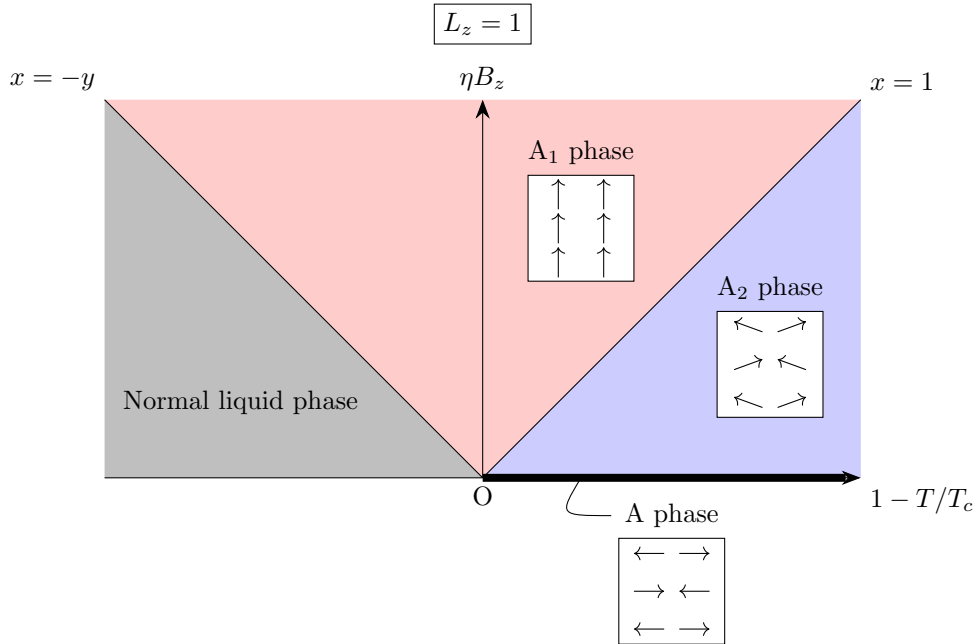


Figure 2. The schematics of the phase diagram focusing on A, A₁, and A₂ phases of the superfluid ³He. Here we fix the orbital angular momentum at $L_z = 1$, so the B and B₁ phases do not appear in this phase diagram. The white box in each phase schematically represents the spin configuration of the Cooper pairs with the magnetic field \vec{B} pointing *down* because of the negative g-factor. Note that the spins are not equally spaced as shown in this figure since the ³He is not a solid in our setup.

nucleus [64], while $\mu_N \simeq 3.2 \times 10^{-8} \text{ eV T}^{-1}$ is the nuclear magneton. This choice of the coefficient is justified by the fact that the spin density is expressed as $\vec{s} \equiv -i(\vec{\phi}^* \times \vec{\phi})$. Indeed, the last term describes the interaction between the magnetic field and the spin of the form $g\mu_N \vec{B} \cdot \vec{s}$.

We can now study the ordering of nuclear spins using $\vec{\phi}$ and its expectation values in different phases. In the A₂ phase, the spin per Cooper pair is calculated as

$$\vec{S} \equiv \frac{\vec{s}}{n} = \begin{pmatrix} 0 \\ 0 \\ x \end{pmatrix}. \quad (2.36)$$

In the limit of $B_z \rightarrow 0$ or $x \rightarrow 0$, this phase is smoothly connected to the A phase, which has an anti-ferromagnetic ordering with $\vec{S} = \vec{0}$. In the A₁ phase, the spin per Cooper pair is

$$\vec{S} = \begin{pmatrix} 0 \\ 0 \\ 1 \end{pmatrix}, \quad (2.37)$$

which shows that the spins of Cooper pairs are completely aligned along the direction of $g\mu_N \vec{B}$. Therefore, we conclude that the A₁ phase has a ferromagnetic ordering.

2.3 Nuclear magnons in the ferromagnetic A_1 phase

Depending on the symmetry-breaking patterns in different phases, there appear several gapless modes, the so-called Nambu-Goldstone (NG) modes. These modes are classified as type-A and type-B modes with characteristic dispersion relations at the long-wavelength limit [65, 66]. For example, in the ferromagnetic A_1 phase, the coset space is given by

$$\mathbb{R}P^3 = \frac{\text{SO}(3)_S \times \text{U}(1)_\phi}{\text{SO}(2)_{S_z - \phi}}, \quad (2.38)$$

which corresponds to one type-A NG mode with a linear dispersion and one type-B NG mode with a quadratic dispersion. The type-B mode is identified as an acoustic magnon mode, whose gap can be generated by the soft symmetry-breaking effect, including the external magnetic field. On the other hand, in the anti-ferromagnetic A_2 phase, the coset space is given by

$$S^2 \times \text{U}(1)_\phi = \frac{\text{SO}(3)_S \times \text{U}(1)_\phi}{\text{SO}(2)_{S_z}}, \quad (2.39)$$

which corresponds to three type-A NG modes, two of which are identified as magnon modes with S_x and S_y . Since the magnon modes in the ferromagnetically-ordered phase have the strongest interaction with the spatially uniform magnetic field, such as the one induced by the axion dark matter, we will focus on the type-B magnon mode in the A_1 phase.

The excitation modes in the superfluid ^3He can be studied by treating the normalized order parameter $\vec{\phi}$ as a dynamical field. The field theory Lagrangian is given by

$$\mathcal{L} = i\vec{\phi}^\dagger \cdot \partial_t \vec{\phi} - \frac{1}{2m^*} \sum_i (\partial_i \vec{\phi}^\dagger) \cdot (\partial_i \vec{\phi}) - V, \quad (2.40)$$

where $i = x, y, z$ are the space coordinates, and the potential V is given by eq. (2.35). The effective mass m^* depends on the pressure imposed on ^3He and can be experimentally determined through measurements of the specific heat. The typical value of m^* is about 3 to 6 times larger than the ^3He atomic mass [67].

In order to study the magnon excitation mode in the A_1 phase, we add a quantum fluctuation $\hat{\psi}$ to the expectation value $\langle \vec{\phi} \rangle = \sqrt{n/2}(1, i, 0)$ as

$$\vec{\phi} = \frac{\sqrt{n}}{2\sqrt{2}} \begin{pmatrix} 2 - \hat{\psi}^\dagger \hat{\psi} - \hat{\psi}^2 \\ i(2 - \hat{\psi}^\dagger \hat{\psi} + \hat{\psi}^2) \\ -2\sqrt{2 - \hat{\psi}^\dagger \hat{\psi} \hat{\psi}} \end{pmatrix}. \quad (2.41)$$

We also consider the fluctuation of the magnetic field as $\vec{B} = (0, 0, -B_z)^T + \delta\vec{B}$ with $B_z > 0$. For simplicity, we assume that both $\hat{\psi}$ and $\delta\vec{B}$ do not depend on the space coordinate. By substituting the expansion in the Lagrangian (2.40) and picking up only the leading-order terms of the fluctuation $\hat{\psi}$ and $\delta\vec{B}$, we obtain the following terms

$$\delta\mathcal{L} = g\mu_N n B_z \hat{\psi}^\dagger \hat{\psi} + \frac{1}{\sqrt{2}} g\mu_N n \left(\delta B_x (\hat{\psi} + \hat{\psi}^\dagger) - i\delta B_y (\hat{\psi} - \hat{\psi}^\dagger) \right), \quad (2.42)$$

which originally come from the last term of the potential (2.35).

It is convenient to discuss in terms of the non-relativistic Hamiltonian described with the magnon operators. For this purpose, we first obtain the relationship of the spin density

$$\hat{s}_+ \equiv \hat{s}_x + i\hat{s}_y = n\sqrt{2 - \hat{\psi}^\dagger \hat{\psi}} \hat{\psi}, \quad (2.43)$$

$$\hat{s}_- \equiv \hat{s}_x - i\hat{s}_y = n\hat{\psi}^\dagger \sqrt{2 - \hat{\psi}^\dagger \hat{\psi}}, \quad (2.44)$$

$$\hat{s}_z = n(1 - \hat{\psi}^\dagger \hat{\psi}). \quad (2.45)$$

On the other hand, using the Holstein–Primakoff transformation with the spin size $s = 1$, we can relate the spin operator of each Cooper pair labeled by ℓ to the magnon annihilation and creation operators as

$$\hat{S}_\ell^+ = \sqrt{2 - \hat{b}_\ell^\dagger \hat{b}_\ell} \hat{b}_\ell, \quad (2.46)$$

$$\hat{S}_\ell^- = \hat{b}_\ell^\dagger \sqrt{2 - \hat{b}_\ell^\dagger \hat{b}_\ell}, \quad (2.47)$$

$$\hat{S}_\ell^z = 1 - \hat{b}_\ell^\dagger \hat{b}_\ell, \quad (2.48)$$

with the canonical commutation relation of bosonic operators $[\hat{b}_\ell, \hat{b}_{\ell'}^\dagger] = \delta_{\ell\ell'}$. We are only interested in the spatially uniform mode obtained by the Fourier transformation $\hat{d} \equiv \sum_{\ell=1}^N \hat{b}_\ell / \sqrt{N}$, where $N \equiv nV_{\text{3He}}$ is the total number of Cooper pairs with V_{3He} being the volume of the superfluid ^3He . We find that this mode is related to the spatially uniform fluctuation $\hat{\psi}$ as

$$\hat{d} = \sqrt{N} \hat{\psi}. \quad (2.49)$$

Note that eq. (2.49) is consistent when $\hat{\psi}$ obeys a bosonic commutation relation, which is the case for the spinor BEC formalism.

Finally, substituting the magnon operator (2.49) in the Lagrangian (2.42), we obtain the relevant part of the Hamiltonian

$$H = \omega_L \hat{d}^\dagger \hat{d} - \sqrt{\frac{N}{2}} g\mu_N \left(\delta B_x (\hat{d} + \hat{d}^\dagger) - i\delta B_y (\hat{d} - \hat{d}^\dagger) \right) + \dots, \quad (2.50)$$

where $\omega_L \equiv -g\mu_N B_z$ is the Larmor frequency. As we will see below, the second term causes the magnon excitation by the axion-induced effective magnetic field.

3 Axion detection

In this section, we discuss the method to obtain the cavity photon signal from the axion. In section 3.1, we will see how the axion is converted into the magnon. In section 3.2, we will look at the mixing between the magnon and the cavity photon. This cavity photon is used as a signal. In section 3.3, we will discuss how to catch the signal with quantum measurement techniques.

3.1 Axion-magnon conversion

As is mentioned above, the spin angular momentum of a ${}^3\text{He}$ nucleus originates from the neutron spin. As a result, the axion-proton coupling can be neglected in our discussion, which generally has a different value from the axion-neutron coupling. The axion-neutron dynamics is described by the Lagrangian

$$\mathcal{L} = \frac{1}{2}(\partial_\mu a)^2 - \frac{1}{2}m_a a^2 + \bar{n}(i\not{\partial} - m_n)n + C_{ann}\frac{\partial_\mu a}{2f_a}\bar{n}\gamma^\mu\gamma_5 n, \quad (3.1)$$

where a and n are the axion and the neutron fields with masses m_a and m_n , respectively, C_{ann} is a model-dependent $\mathcal{O}(1)$ coupling coefficient, and f_a is the axion decay constant. For the QCD axion, there is a relationship between m_a and f_a [68]:

$$m_a \simeq 5.7 \mu\text{eV} \times \left(\frac{10^{12} \text{ GeV}}{f_a} \right). \quad (3.2)$$

We assume that the axion field explains all of the dark matter abundance through the misalignment mechanism [3, 69, 70]; accordingly, the axion field can be treated as a classical field with coherent oscillation

$$a(t, \vec{x}) \simeq a_0 \sin(m_a t - m_a \vec{v}_a \cdot \vec{x} + \varphi), \quad (3.3)$$

where v_a is the velocity of axion, while φ is a random phase. Here, we utilize the fact that the axion is non-relativistic to approximate the axion energy to be m_a . Using these variables, the local dark matter density $\rho_a \sim 0.45 \text{ GeV}/\text{cm}^3$ can be expressed as $\rho_a = (m_a a_0)^2/2$. The expression of $a(t, \vec{x})$ tells us that the coherent length of the axion field is given by $\lambda_a \equiv 1/(m_a v_a)$. Since $\lambda_a \sim 100 \text{ m}$ for $m_a \sim 1 \mu\text{eV}$ and $v_a \sim 10^{-3}$ [71], the axion field can be regarded as a spatially uniform field within an experimental apparatus, which allows us to neglect the second argument of the sine function. Also, the coherence time of the axion field is $\tau_a \simeq 1/(m_a v_a^2) \sim 1 \text{ ms}$ for $m_a \sim 1 \mu\text{eV}$, during which the velocity \vec{v}_a and the phase φ can be treated as constant.

In the non-relativistic limit, we obtain the following effective Hamiltonian density describing the axion-nucleus interaction:

$$\mathcal{H}_{\text{eff}} \simeq -C_{ann} \frac{m_a a_0}{f_a} \vec{v}_a \cdot \vec{s}_N \sin(m_a t + \varphi), \quad (3.4)$$

where \vec{s}_N is the spin density operator of ${}^3\text{He}$ nuclei, which can be identified as the spin operator of neutrons in the ${}^3\text{He}$. Note that the interaction strength is proportional to $m_a a_0 = \sqrt{2\rho_a}$ and independent of m_a . The interaction term can be rewritten in the form of the ordinary spin-magnetic field coupling, $\mathcal{H} = \gamma_N \vec{B}_a \cdot \vec{s}_N \sin(m_a t + \varphi)$, where $\gamma_N = g\mu_N$ is the gyromagnetic ratio of a nucleus. The effective axion magnetic field that exclusively couples to the neutron spins is given by

$$\gamma_N \vec{B}_a(t) = -C_{ann} \frac{\sqrt{2\rho_a}}{f_a} \vec{v}_a \sin(m_a t + \varphi). \quad (3.5)$$

Thus, by substituting $\delta\vec{B}$ by \vec{B}_a in eq. (2.50), we obtain the Hamiltonian of the axion-nuclear magnon coupled system

$$H(t) = H_0 + H_{\text{int}}(t), \quad (3.6)$$

$$H_0 = \omega_L \hat{d}^\dagger \hat{d}, \quad (3.7)$$

$$H_{\text{int}}(t) = \frac{C_{\text{ann}}}{f_a} \sqrt{\rho_a N} \left(v_a^+ \hat{d}^\dagger + \text{h.c.} \right) \sin(m_a t + \varphi), \quad (3.8)$$

where $v_a^+ \equiv v_a^x + i v_a^y$.

We define the ground state $|0\rangle$ and the one-magnon state $|1\rangle$ of ${}^3\text{He}$ with $\hat{d}|0\rangle = 0$ and $|1\rangle \equiv \hat{d}^\dagger|0\rangle$.² Then, the magnon production amplitude is calculated as

$$-i\mathcal{M} = \langle 1|U(t)|0\rangle = -i \int_0^t dt' \langle 1|H_{\text{int}}(t')|0\rangle e^{-i\omega_L t'}, \quad (3.9)$$

where $t < \tau_a$ is the observation time and the evolution matrix is defined as

$$U(t) \equiv \exp \left[-i \int_0^t dt' H(t') \right]. \quad (3.10)$$

Since the axion spectrum is approximately monochromatic with energy m_a , the magnon production rate is resonantly enhanced when $m_a = \omega_L$. In this limit, the amplitude is evaluated as

$$\mathcal{M} \simeq -i \frac{C_{\text{ann}}}{2f_a} \sqrt{\rho_a N} v_a^+ e^{i\varphi} t, \quad (3.11)$$

where we assumed $t \gg \omega_L^{-1}$ so that the oscillatory term can be dropped. Then the transition probability is

$$P = |\mathcal{M}|^2 = \left(\frac{C_{\text{ann}}}{2f_a} \right)^2 \rho_a N t^2 v_a^2 \sin^2 \theta_a, \quad (3.12)$$

where θ_a is the relative angle between the external magnetic field and axion wind. This result is consistent with [72] where the spatially uniform mode (the Kittel mode) of the electronic magnons is considered.

The transition probability grows as $P \propto t^2$ as far as the coherence of the signal is maintained. The typical coherence time τ can be estimated as

$$\tau \sim \min(\tau_a, \tau_{\text{mag}}, \tau_{\text{exp}}), \quad (3.13)$$

where τ_{mag} is the lifetime of magnon, and τ_{exp} denotes the minimum relaxation time scale of excitation modes used for the magnon detection. Since we propose to use the mixing between a nuclear magnon and a cavity photon as is discussed in section 3.2, the cavity quality factor Q is an important component that determines τ_{exp} . In this paper, we can use the relationship $\tau_{\text{mag}} < \tau_a$ since $\tau_{\text{mag}} \sim 1.2 \mu\text{s}$ [73], while $\tau_a \sim 1 \text{ ms}$ for the parameter

²States with more than one magnon can be safely neglected due to the smallness of the magnon excitation rate for the axion parameter region of our interest.

region of our interest. Also, we assume $\tau_{\text{mag}} < \tau_{\text{exp}}$ and use $\tau = \tau_{\text{mag}}$ for the following calculation, which is reasonable for $Q \gtrsim 10^3$.

Finally, the signal rate for the total observation time $t \gg \tau$ is evaluated as

$$\frac{dN_{\text{sig}}}{dt} = \frac{N}{4} C_{\text{ann}}^2 \frac{\rho_a v_a^2 \sin^2 \theta_a}{f_a^2} \tau, \quad (3.14)$$

where $\sin^2 \theta_a$ should be replaced by the averaged value if $t \gg \tau_a$. Hereafter, we assume this is the case and simply average out the directional dependence, though it might be interesting to study it further in light of the modulation of the axion signal. Note that the total number of Cooper pairs for ${}^3\text{He}$ of mass M is calculated as $N = M/(2m_{{}^3\text{He}}) \sim 1.0 \times 10^{25} (M/100 \text{ g})$. For the QCD axion, for example, the external magnetic field $B_z = 10 \text{ T}$ corresponds to the Larmor frequency $\omega_L = m_a \simeq 1.3 \mu\text{eV}$ and $f_a \simeq 4.3 \times 10^{12} \text{ GeV}$, which result in

$$\frac{dN_{\text{sig}}}{dt} = 8.7 \times 10^{-6} \text{ s}^{-1} \times C_{\text{ann}}^2 \left(\frac{M}{100 \text{ g}} \right) \left(\frac{v_a}{10^{-3}} \right)^2. \quad (3.15)$$

For later convenience, we also show the expression of the signal power:

$$P_{\text{sig}} = 1.9 \times 10^{-31} \text{ W} \times C_{\text{ann}}^2 \left(\frac{M}{100 \text{ g}} \right) \left(\frac{v_a}{10^{-3}} \right)^2 \sin^2 \theta_a. \quad (3.16)$$

3.2 Mixing between magnon and cavity modes

When one of the cavity modes has the same frequency as the magnons of our interest, $\omega_{\text{cavity}} = \omega_L$, there is a large mixing between these modes. This can be understood similarly as the formation of the magnon-polariton of electron spins [74–76]. Let \hat{c} (\hat{c}^\dagger) be the annihilation (creation) operator of the cavity mode. Assuming that all the other cavity modes have frequencies largely deviated from ω_L , we can safely neglect them and write down the relevant part of the Hamiltonian

$$H = \omega_L \hat{d}^\dagger \hat{d} + \omega_{\text{cavity}} \hat{c}^\dagger \hat{c} + H_{\text{mix}}. \quad (3.17)$$

The mixing term is sourced from the interaction between nucleon spin and the magnetic field of the cavity mode and is given by

$$H_{\text{mix}} = ig\mu_N \int_{{}^3\text{He}} dV \left(\vec{\phi}^*(\vec{r}) \times \vec{\phi}(\vec{r}) \right) \cdot \vec{B}_0(\vec{r}) (\hat{c} + \hat{c}^\dagger), \quad (3.18)$$

where the volume integral is performed over the volume of the superfluid ${}^3\text{He}$, while $\vec{B}_0(\vec{r})$ is the profile of the magnetic field of the cavity mode. If we consider as an example the cavity mode with $\vec{B}_0(\vec{r}) = B_0(\vec{r}) \vec{u}_x$ with \vec{u}_x being the unit vector along the x -axis, terms linear in the magnon mode is obtained similarly to eq. (2.50) as

$$H_{\text{mix}} \simeq \sqrt{\frac{N}{2}} g\mu_N \bar{B}_0 (\hat{d} + \hat{d}^\dagger) (\hat{c} + \hat{c}^\dagger), \quad (3.19)$$

where the averaged magnetic field over the superfluid ^3He is defined as

$$\bar{B}_0 \equiv \frac{1}{V_{^3\text{He}}} \int_{^3\text{He}} dV B_0(\vec{r}). \quad (3.20)$$

We finally find the quadratic part of the Hamiltonian

$$H \simeq \omega_L \hat{d}^\dagger \hat{d} + \omega_{\text{cavity}} \hat{c}^\dagger \hat{c} + g_{\text{eff}} (\hat{c} \hat{d}^\dagger + \hat{c}^\dagger \hat{d}), \quad (3.21)$$

$$g_{\text{eff}} = \sqrt{\frac{N}{2}} g \mu_N \bar{B}_0, \quad (3.22)$$

where we used the rotating wave approximation to neglect the fast oscillation terms. Note that the typical size of the magnetic field can be estimated by matching the electromagnetic energy with a cavity mode frequency. Defining $\langle B_0^2 \rangle \equiv \frac{1}{V_{\text{cavity}}} \int_{\text{cavity}} dV B_0^2(\vec{r})$ with integration over the cavity volume, we obtain

$$\sqrt{\langle B_0^2 \rangle} \sim 4 \text{fT} \left(\frac{\omega_{\text{cavity}}}{10^2 \text{MHz}} \right)^{1/2} \left(\frac{10^3 \text{cm}^3}{V_{\text{cavity}}} \right)^{1/2}. \quad (3.23)$$

For the order estimation of the physics scales, we can approximate that $\bar{B}_0 \sim \sqrt{\langle B_0^2 \rangle}$, though there can be an $\mathcal{O}(1)$ geometry factor difference. Indeed, this estimation is consistent with [76], which shows that $\bar{B}_0 \sim 5 \text{pT}$ in one of the figures, while a rough estimation gives $\sqrt{\langle B_0^2 \rangle} \sim 1 \text{pT}$.

By diagonalizing the Hamiltonian (3.21), we obtain the energy eigenstates. In particular, the maximal mixing is realized when $\omega_L = \omega_{\text{cavity}}$ with the corresponding energy eigenvalues $|\omega_L \pm g_{\text{eff}}|$. Compared with the magnon-polariton of electron spins, the energy scale of the system is smaller by a factor of $\mu_N/\mu_B \sim 10^{-3}$ with μ_B being the Bohr magneton. This affects the time scale of the conversion of the magnon mode into the cavity mode. The time scale can be estimated by evaluating the energy gap $\Delta E = 2 \min(\omega_L = \omega_{\text{cavity}}, g_{\text{eff}})$ between two energy eigenstates. Assuming $V_{^3\text{He}} \sim V_{\text{cavity}}$ for simplicity, and the above estimation of \bar{B}_0 , we have

$$\frac{g_{\text{eff}}}{2\pi} \sim 0.3 \text{MHz} \left(\frac{M}{100 \text{g}} \right)^{1/2} \left(\frac{\omega_L}{10^2 \text{MHz}} \right)^{1/2}, \quad (3.24)$$

where the $\omega_L = \omega_{\text{cavity}}$ dependence comes from that of $\sqrt{\langle B_0^2 \rangle}$. This expression, together with $\omega_L \sim 200 \text{MHz}$ for $B = 1 \text{T}$, shows that the conversion time scale, which is usually fixed by $g_{\text{eff}} < \omega_L$, can be comparable to or shorter than the magnon lifetime $\tau_{\text{mag}} \sim 1.2 \mu\text{s}$. Thus, it is expected that a sizable fraction of magnons excited by the axion DM is converted to and detected as cavity modes. In appendix A, we show the detailed calculation of the dynamics of the magnon-cavity mixed system including various loss factors and quantum measurement techniques briefly introduced in the next subsection.

3.3 Quantum measurement techniques

In general, if one wants to detect weak signals originating from axions, it is helpful to amplify those signals with some amplifier. In such a case, the noise consists of two main

contributions: the thermal noise and the noise from the amplifier. By expressing these noises in terms of temperatures, the total noise $k_B T_N$ is written as [77]

$$k_B T_N = \omega \left(n_T + \frac{1}{2} \right) + k_B T_A, \quad (3.25)$$

where $k_B T_A$ is the noise from the amplifier, and n_T is the occupation number of thermal photons under the physical temperature T (the temperature of the cavity in our setup),

$$n_T = \frac{1}{\exp\left(\frac{\omega}{k_B T}\right) - 1}. \quad (3.26)$$

Even at zero temperature, the noise has a nonzero value, which is known as the standard quantum limit (SQL),

$$k_B T_{\text{SQL}} = \omega. \quad (3.27)$$

Half of $k_B T_{\text{SQL}}$ comes from the thermal noise, and the other half comes from $k_B T_A$. For instance, $T_{\text{SQL}} \sim 48$ mK at $\omega \sim 1$ GHz. This SQL can be circumvented by using quantum measurement techniques (see [78] for a review). We use the squeezing of states and the homodyne measurement as described in [39]. We will summarize these techniques in this subsection.

3.3.1 Squeezing of states

The starting point is introducing *quadratures* \hat{X} and \hat{Y} defined in terms of the annihilation (creation) operator of photons \hat{a} (\hat{a}^\dagger) as

$$\hat{X} \equiv \frac{\hat{a} + \hat{a}^\dagger}{\sqrt{2}}, \quad \hat{Y} \equiv \frac{\hat{a} - \hat{a}^\dagger}{\sqrt{2}i}. \quad (3.28)$$

Because of the commutation relation $[\hat{a}, \hat{a}^\dagger] = 1$, quadratures satisfy $[\hat{X}, \hat{Y}] = i$. This commutation relation results in the uncertainty relation of quadratures

$$(\Delta \hat{X})^2 (\Delta \hat{Y})^2 \geq \frac{1}{4}. \quad (3.29)$$

Since many of the ordinary measurement techniques measure both quadratures of the input signal at each time, the quantum noise $\Delta \hat{X} \sim \Delta \hat{Y} \sim 1/2$ must appear and contribute to the SQL. However, quantum measurement techniques can decrease this quantum noise by focusing on only one of the quadratures. For example, a larger part of the uncertainty can be imposed on \hat{Y} , as $\Delta \hat{X} \sim 1/(2\sqrt{G})$ and $\Delta \hat{Y} \sim \sqrt{G}/2$ with $G \gg 1$, which reduces the uncertainty on the observable \hat{X} and remains consistent with eq. (3.29). This operation is called squeezing. Squeezing can be performed by, e.g., phase-sensitive amplifiers such as Josephson parametric amplifiers (JPAs); see appendix B for details.

A possible experimental setup, which is similar to the setup of the HAYSTAC experiment [12–14], is schematically shown in fig. 3. We also summarize in fig. 4 how the state is squeezed in the XY plane. In this setup, squeezing is performed twice by JPAs. First,

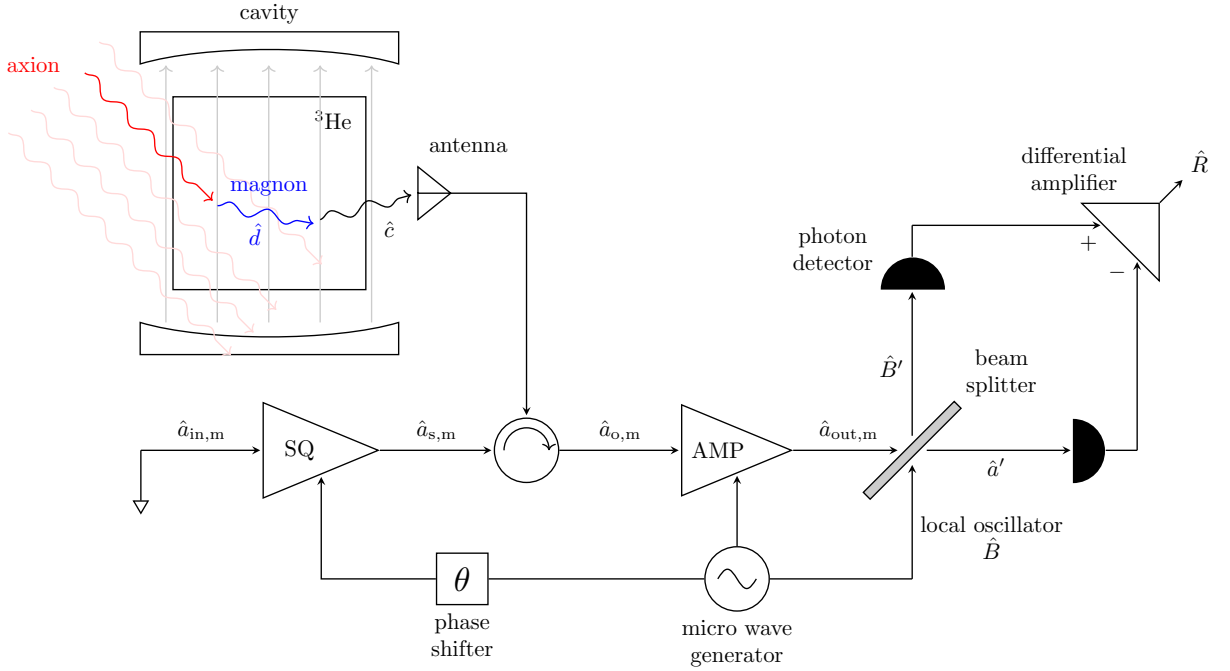


Figure 3. Schematic of our experimental setup for axion detection with superfluid ${}^3\text{He}$. The operators $\hat{c}, \hat{d}, \hat{B}, \dots$ correspond to the annihilation operators used in our paper.

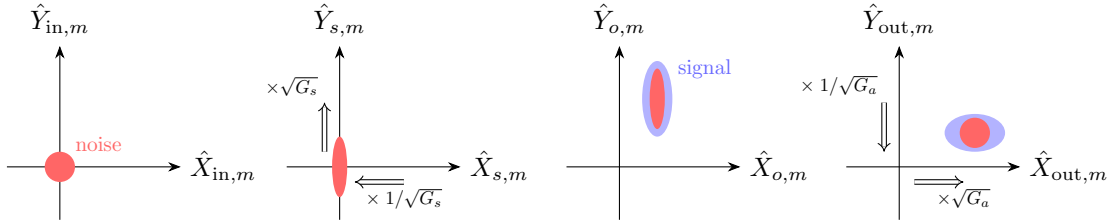


Figure 4. Distribution of the four states in the XY plane. The subscripts of quadratures correspond to those in fig. 3. The input state $(\hat{X}_{\text{in},m}, \hat{Y}_{\text{in},m})$ is Gaussian, which is the distribution of thermal photons. This state will be squeezed by the SQ JPA and becomes the squeezed state $(\hat{X}_{s,m}, \hat{Y}_{s,m})$. The third state $(\hat{X}_{o,m}, \hat{Y}_{o,m})$ is the state after the signal from the cavity is received. Finally, we get the output state $(\hat{X}_{\text{out},m}, \hat{Y}_{\text{out},m})$ after squeezing by the AMP JPA.

we assume that the input vacuum state $(\hat{X}_{\text{in},m}, \hat{Y}_{\text{in},m})$ ³ is the coherent state, which is the case for the thermal photons with a Gaussian distribution in the XY plane. The first JPA called SQ in fig. 3 squeezes the vacuum state along, e.g., the X direction. When we define the squeezing parameter of the SQ JPA as G_s , the squeezed state $(\hat{X}_{s,m}, \hat{Y}_{s,m})$ becomes

$$\hat{X}_{s,m} = \frac{1}{\sqrt{G_s}} \hat{X}_{\text{in},m}, \quad \hat{Y}_{s,m} = \sqrt{G_s} \hat{Y}_{\text{in},m}. \quad (3.30)$$

This squeezing reduces the noise $\Delta \hat{X}$.

³The meaning of subscript m is described in appendix A.

When this squeezed state receives the signal photon from the cavity, the state is displaced in the phase of the signal photon (from the second figure to the third figure in fig. 4). Because the noise has been suppressed by a factor $1/\sqrt{G_s}$, the signal-to-noise ratio is enhanced by a factor $\sqrt{G_s}$. The second JPA called AMP squeezes the displaced state $(\hat{X}_{o,m}, \hat{Y}_{o,m})$. This JPA amplifies the state in the X direction, the opposite direction to the SQ, and we get the output state $(\hat{X}_{out,m}, \hat{Y}_{out,m})$. Defining the squeezing parameter of the AMP JPA as G_a , we get

$$\hat{X}_{out,m} = \sqrt{G_a} \hat{X}_{o,m}, \quad \hat{Y}_{out,m} = \frac{1}{\sqrt{G_a}} \hat{Y}_{o,m}. \quad (3.31)$$

Note that this second squeezing does not affect the signal-to-noise ratio because it amplifies both the signal and noise at the same time. Instead, the AMP JPA plays a role in overwhelming the noise added by the following circuits, including the amplifier.

Technically, the direction of squeezing by JPAs is determined by the phase of the AC power input to them. In order to give a difference to the direction of amplification by the SQ and AMP JPA, the phase shifter between the microwave generator and the SQ JPA shifts the phase of the microwaves by $\pi/2$.

3.3.2 Homodyne measurement

Now we need to measure the \hat{X} quadrature exclusively to obtain a high signal-to-noise ratio beyond the SQL. This is possible by using another quantum measurement technique, the homodyne measurement. We will briefly review the theory of the homodyne measurement. A schematic of the homodyne measurement is shown in the lower right part of fig. 3.

First, let $|\psi\rangle$ be the signal state of our setup, i.e., the squeezed state output from the AMP JPA. Also, in this subsection, we use the abbreviation for notation of the corresponding annihilation operator and quadratures, \hat{a} , \hat{X} , and \hat{Y} , representing $\hat{a}_{out,m}$, $\hat{X}_{out,m}$, and $\hat{Y}_{out,m}$, respectively. The homodyne measurement requires a local oscillator that has the same mode as that of the signal photons. We write the annihilation operator of the local oscillator by \hat{B} , and set the initial state of the local oscillator to a coherent state

$$|\beta\rangle \equiv e^{-|\beta|^2/2} \sum_{n=0}^{\infty} \frac{\beta^n}{\sqrt{n!}} |n\rangle. \quad (3.32)$$

Here, $\beta \equiv |\beta|e^{i\theta}$ and $|n\rangle$ is the Fock state of n photons. The initial state of the total system is defined as $|\Psi\rangle \equiv |\psi\rangle |\beta\rangle$.

The signal photons and the local oscillator are split in half and mixed by a beam splitter. As a result, we obtain two beams whose annihilation operators are

$$\hat{a}' = \frac{\hat{a} - \hat{B}}{\sqrt{2}}, \quad \hat{B}' = \frac{\hat{a} + \hat{B}}{\sqrt{2}}. \quad (3.33)$$

Next, we observe the difference \hat{R} between the amplitudes of those two beams by a differential amplifier:

$$\begin{aligned} \hat{R} &\equiv \hat{B}'^\dagger \hat{B}' - \hat{a}'^\dagger \hat{a}' \\ &= \frac{\hat{a} + \hat{a}^\dagger}{\sqrt{2}} \frac{\hat{B} + \hat{B}^\dagger}{\sqrt{2}} + \frac{\hat{a} - \hat{a}^\dagger}{\sqrt{2}i} \frac{\hat{B} - \hat{B}^\dagger}{\sqrt{2}i}. \end{aligned} \quad (3.34)$$

The expectation value of \hat{R} is calculated as

$$\begin{aligned}\langle \Psi | \hat{R} | \Psi \rangle &= \langle \psi | \left(\frac{\hat{a} + \hat{a}^\dagger}{\sqrt{2}} \frac{\beta + \beta^*}{\sqrt{2}} + \frac{\hat{a} - \hat{a}^\dagger}{\sqrt{2}i} \frac{\beta - \beta^*}{\sqrt{2}i} \right) | \psi \rangle \\ &= \sqrt{2} |\beta| \langle \psi | (\hat{X} \cos \theta + \hat{Y} \sin \theta) | \psi \rangle.\end{aligned}\quad (3.35)$$

This equation means that we can measure only one component of quadratures by observing \hat{R} . For example, if $\theta = 0$, we can measure only the \hat{X} quadrature. If we tune the phase θ to be the same as the phase of amplification by the AMP JPA, we can measure only the amplified quadrature. This tuning is possible by using the same microwave generator for the AMP JPA and the local oscillator of the homodyne measurement; see fig. 3. Thus, the expectation value of the normalized observable $\hat{R}' \equiv \hat{R}/\sqrt{2}|\beta|$ becomes

$$\langle \Psi | \hat{R}' | \Psi \rangle = \langle \psi | \hat{X} | \psi \rangle. \quad (3.36)$$

Furthermore, the measurement error of the operator \hat{R}' is

$$\langle \Psi | (\hat{R}' - \hat{X})^2 | \Psi \rangle = \frac{\langle \psi | \hat{a}^\dagger \hat{a} | \psi \rangle}{2|\beta|^2}, \quad (3.37)$$

which converges to zero in the limit of $|\beta| \rightarrow \infty$. Therefore, \hat{X} can be accurately measured through the homodyne measurement using the local oscillator with a large number of photons.

4 Sensitivity

We determine the sensitivity of our setup using a similar test statistic as the one used in [34] in a limit where the signal power is considerably smaller than the noise power. Here, we briefly outline our statistical analysis, leaving details of calculations to appendix A. In order to determine the 95% exclusion limits by a log-likelihood ratio test statistic, we calculate the following quantity

$$q \equiv -\frac{T_{\text{int}}}{2\pi} \int_0^\infty d\omega \frac{S(\Delta\omega)^2}{B(\Delta\omega)^2}, \quad (4.1)$$

where T_{int} is the experimental integration time, $\Delta\omega \equiv \omega - \omega_L$, and $S(\Delta\omega)$ and $B(\Delta\omega)$ are the signal and the noise spectral density, respectively. The 95% exclusion limits are obtained by solving $q = -2.71$.

According to the calculation in appendix A, we obtain

$$q \simeq \begin{cases} -6.9 \times 10^{58} g_{\text{ann}}^4 \left(\frac{T_{\text{int}}}{1 \text{ day}} \right) \left(\frac{m_a}{1 \text{ } \mu\text{eV}} \right)^{-7/2} \left(\frac{G_s}{10^2} \right)^{1/2} \left(\frac{M}{100 \text{ g}} \right)^2 \left(\frac{Q}{10^{11}} \right)^{3/2} \\ \quad \text{for } Q/G_s \gtrsim 1.1 \times 10^8 \\ -2.5 \times 10^{49} g_{\text{ann}}^4 \left(\frac{T_{\text{int}}}{1 \text{ day}} \right) \left(\frac{m_a}{1 \text{ } \mu\text{eV}} \right)^{-3} \left(\frac{M}{100 \text{ g}} \right)^2 \left(\frac{Q}{10^6} \right)^2 \\ \quad \text{for } Q/G_s \lesssim 1.1 \times 10^8 \end{cases}, \quad (4.2)$$

where we defined the dimensionless coupling $g_{ann} \equiv C_{ann} m_n / f_a$. Equation (4.2) shows that q does not depend on G_s when $Q/G_s \lesssim 1.1 \times 10^8$, i.e., the sensitivity cannot be improved by the squeezing unless we achieve high Q/G_s . Note that since the cavity is placed under a low temperature $T < T_c \sim \mathcal{O}(1)$ mK, the sensitivity does not depend on T but is limited by the quantum fluctuation. Solving $q = -2.71$, we estimate the expected exclusion limits on the axion-neutron coupling as

$$g_{ann} \simeq \begin{cases} 2.5 \times 10^{-15} \left(\frac{T_{\text{int}}}{1 \text{ day}} \right)^{-1/4} \left(\frac{m_a}{1 \text{ } \mu\text{eV}} \right)^{7/8} \left(\frac{G_s}{10^2} \right)^{-1/8} \left(\frac{M}{100 \text{ g}} \right)^{-1/2} \left(\frac{Q}{10^{11}} \right)^{-3/8} \\ \quad \text{for } Q/G_s \gtrsim 1.1 \times 10^8 \\ 5.7 \times 10^{-13} \left(\frac{T_{\text{int}}}{1 \text{ day}} \right)^{-1/4} \left(\frac{m_a}{1 \text{ } \mu\text{eV}} \right)^{3/4} \left(\frac{M}{100 \text{ g}} \right)^{-1/2} \left(\frac{Q}{10^6} \right)^{-1/2} \\ \quad \text{for } Q/G_s \lesssim 1.1 \times 10^8 \end{cases} . \quad (4.3)$$

In our setup, we scan the magnetic field B_z and the cavity size so that the axion dark matter with mass $m_a \simeq \omega_L = \omega_{\text{cavity}}$ can be searched for. Each scan step has a sensitivity on the axion mass width $\sim 1/\tau$ around the Larmor frequency

$$m_a \sim 0.13 \text{ } \mu\text{eV} \left(\frac{B_z}{1 \text{ T}} \right). \quad (4.4)$$

For simplicity, we approximate the sensitivity curve for each scan by a rectangle with width $1/\tau_{\text{mag}}$ instead of using a Breit-Wigner shape. The typical size of the cavity L_{cavity} is estimated by evaluating the corresponding Compton length as

$$L_{\text{cavity}} \sim 1.2 \text{ m} \left(\frac{1 \text{ } \mu\text{eV}}{m_a} \right). \quad (4.5)$$

The upper limit of the axion mass that can be searched by our experiment is determined by the upper limit of the magnetic field B_z . We adopt 25 T as the maximum of B_z , which can be regarded as realistic as planned for example in CAPP25T by IBS/BNL [79].⁴

The squeezing level G_s is also crucial for sensitivity estimation. Here, we summarize the current status of the squeezing level in various experiments including the gravitational wave telescope. The squeezing levels are usually represented in the unit of dB, and x dB of squeezing corresponds to $G_s = 10^{x/10}$ in our setup. In the context of the gravitational wave detection, 6 dB quantum noise reduction (corresponding to $G_s = 10^{0.6}$) has already been reported [81], while the HAYSTAC experiment of the axion dark matter detection has achieved 4 dB [14]. Even larger values have already been achieved for the squeezed state production of light, such as 8 dB for the microwave and the terahertz range [82, 83], and 15 dB for the megahertz range [84].

It is notable, however, that a hindrance to using the squeezing state for the quantum measurement is the optical loss, which is one of the main obstacles that we have to tackle to improve the sensitivity further (see the discussion in section 5).

⁴As a more optimistic option, ~ 45 T is also planned to be developed [80].

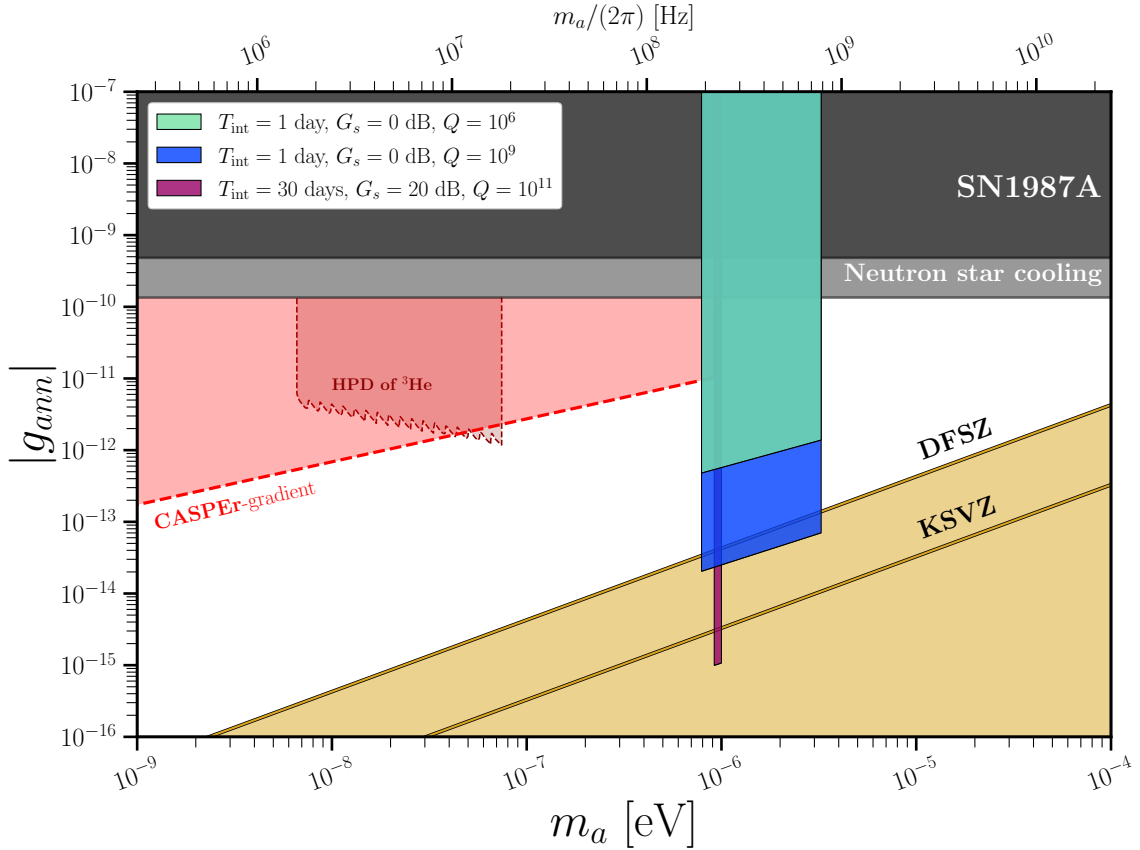


Figure 5. The 95% exclusion limit on the axion-neutron coupling g_{ann} . We plotted the sensitivities for three setups, all of which are operated with the mass of the superfluid ${}^3\text{He}$ target $M = 100$ g, the scan width $1/\tau = 1/\tau_{\text{mag}} \simeq 0.8$ MHz, and the total integration time $T_{\text{tot}} = 2$ years. The green plot shows the sensitivity for a realistic setup with the integration time for each scan $T_{\text{int}} = 1$ day, and the cavity’s quality factor $Q = 10^6$, without quantum measurements. The blue plot shows the same setup as the green one but with a higher-quality cavity, $Q = 10^9$. The feasible upper limit of the magnetic field $B_z = 25$ T corresponds to the upper limits of the axion mass $m_a \simeq 3.25 \mu\text{eV}$ for both cases. The magenta plot is for an ideal setup with $T_{\text{int}} = 30$ days, and $Q = 10^{11}$ in addition to the quantum measurement techniques with the squeezing factor $G_s = 20$ dB. The upper limit of the axion mass for this case is set to $m_a = 1 \mu\text{eV}$. We also plotted the region already constrained by stellar physics [85, 86], the prospects of the CASPER-gradient experiment [26] and the proposal with the homogeneous precession domain [33], the prediction of the DFSZ model with $0.28 \lesssim \tan \beta \lesssim 140$, and that of the KSVZ model. This figure is made by using the public code [87].

In fig. 5, We show the 95% exclusion limits on the axion-neutron coupling g_{ann} with three setups under the total integration time $T_{\text{tot}} = 2$ years. The green region shows the sensitivity of a realistic setup for the axion search; $T_{\text{int}} = 1$ day, $M = 100$ g, and $Q = 10^6$, and quantum measurement techniques are not applied ($G_s = 0$ dB). This setup corresponds to the case of $Q/G_s < 1.1 \times 10^8$. The blue region represents an example of the high- Q/G_s setup; $T_{\text{int}} = 1$ day, $M = 100$ g, $G_s = 0$ dB, and $Q = 10^9$. In both examples, we scan the magnetic field within the range $6.0 \text{ T} \lesssim B_z \lesssim 25 \text{ T}$ with a fixed scan step width

$\Delta B_z \simeq 2.6 \times 10^{-2}$ T corresponding to the axion mass width $1/\tau = 1/\tau_{\text{mag}}$.

If future experiments succeed in discovering axion through its interaction with photons and/or electrons and its mass is already known, our experiment will also help to investigate the axion interaction with neutrons. For this purpose, we do not need to scan a wide mass range, but instead, we can spend a long integration time with a fixed size of magnetic field corresponding to the discovered axion mass. We show the sensitivity of a setup aimed at this purpose in fig. 5 with a longer integration time $T_{\text{int}} = 30$ days, a larger amount of ^3He ($M = 100$ g), the use of squeezing ($G_s = 20$ dB), and a higher-quality cavity ($Q = 10^{11}$). Note that such a high- Q cavity has been achieved using nitrogen doping for superconducting niobium cavities [88]. These values should be understood as an ultimate goal to be achieved to detect the QCD axion-like interaction with neutrons of the DFSZ axion with $\sin\beta \sim \mathcal{O}(1)$ and of the KSVZ axion.

5 Conclusion and Discussion

In this paper, we proposed to use the nuclear magnon modes in the ferromagnetic A_1 phase of the superfluid ^3He for the axion dark matter detection. We stressed the importance of this approach as a way to detect the axion-nucleon coupling, which is one of the most important features of the QCD axion. As a detection method of the nuclear magnon, we proposed to use the mixing between the magnon and the cavity photon modes, which then allows us to use quantum measurement technologies such as squeezing and the homodyne measurement to enhance the dark matter-induced signal. We showed the quantum mechanical description of our approach and derived the corresponding sensitivity on the axion-neutron coupling g_{ann} . As shown in section 4, quantum measurement technologies turned out to be useful for enhancing the sensitivity to weak signals induced by the axion dark matter when we have a high-quality cavity. As a result, we obtained a sensitivity to axion with $\mathcal{O}(1)$ μeV mass under a realistic setup, which exceeds the current best constraints by stellar physics.

Our ideal setup in section 4 relies on the high-squeezing technology that has potential to enhance the signal significance by orders of magnitude. Currently, the squeezing parameter G_s has reached 15 dB [84], and it is expected that the practical use of 20 dB will be achieved in the near future [89]. However, the squeezing effect is suppressed when there is a transmission loss. For example, when we identify the transmission efficiency between the SQ JPA and the cavity and that between the cavity and the AMP JPA as λ , the effective squeezing parameter S becomes

$$S \simeq \left(1 - \lambda + \frac{\lambda}{G_s}\right)^{-1}, \quad (5.1)$$

as shown in [39]. Thus, even in the limit of $G_s \rightarrow \infty$, S plateaus to $(1 - \lambda)^{-1}$. Therefore, almost lossless transmission ($\lambda \simeq 1$) should be developed in order to make full use of the squeezing technology and enhance the sensitivity further.

Finally, we comment that there are several other quantum measurement technologies that can also be applied to the dark matter detection. These technologies include two mode

squeezing and state swapping interactions [40, 45]. For a higher frequency range, single photon counting is also a viable approach [46]. There is an attempt using superconducting qubits, which have reduced the noise to 15.7 dB below the standard quantum limit through the repeated quantum non-demolition measurements [44].

Acknowledgements

We thank Yoji Ohashi and Masahito Ueda for giving advice on the superfluid ^3He , and Yuta Michimura for information about the quantum technology of gravitational wave detectors and the likely achievements in squeezing. RO also thanks Satoshi Shirai and Keiichi Watanabe for pointing out a typo in the sensitivity calculation. SC and HM are supported by the Director, Office of Science, Office of High Energy Physics of the U.S. Department of Energy under the Contract No. DE-AC02-05CH1123. RO and HS are supported by Forefront Physics and Mathematics Program to Drive Transformation (FoPM), a World-leading Innovative Graduate Study (WINGS) Program, the University of Tokyo. DK and HM are supported by the Beyond AI Institute, the University of Tokyo. HM is also supported in part by the NSF grant PHY-2210390, by the JSPS Grant-in-Aid for Scientific Research JP20K03942, MEXT Grant-in-Aid for Transformative Research Areas (A) JP20H05850, JP20A203, by WPI, MEXT, Japan, and Hamamatsu Photonics, K.K.

A Statistical treatment of noise

A.1 Formulation

In this section, we derive the expression eq. (4.2) of our test statistic q . This quantity has been introduced as a parameter for a log-likelihood ratio test in [34]. We consider a quantum formulation of our system including the magnon and the cavity modes and apparatuses for squeezing and the homodyne measurement, and use it to evaluate the signal and the background spectral densities. We start with the following Hamiltonian for the cavity mode \hat{c} and background modes interacting with the cavity mode:

$$H_{\text{tot}} = H_{\text{sys}} + H_{\text{int}} + H_{\text{B}}, \quad (\text{A.1})$$

$$H_{\text{sys}} = \omega_L \hat{c}^\dagger \hat{c} + \omega_L \hat{d}^\dagger \hat{d} - i \frac{\Gamma_{\text{mag}}}{2} \hat{d}^\dagger \hat{d} + i g_{\text{eff}} (\hat{c}^\dagger \hat{d} - \hat{c} \hat{d}^\dagger), \quad (\text{A.2})$$

$$H_{\text{int}} = i \sum_{j=m,l} \sqrt{\frac{\kappa_j}{2\pi}} \int d\omega \left[\hat{c}^\dagger \hat{a}_j(\omega) - \hat{c} \hat{a}_j^\dagger(\omega) \right] + i \sqrt{\frac{\kappa_a}{2\pi}} \int d\omega \left[\hat{d}^\dagger \hat{a}_a(\omega) - \hat{d} \hat{a}_a^\dagger(\omega) \right], \quad (\text{A.3})$$

$$H_{\text{B}} = \sum_{j=m,l,a} \int d\omega \omega \hat{a}_j^\dagger(\omega) \hat{a}_j(\omega), \quad (\text{A.4})$$

where \hat{d} is the annihilation operator of magnon defined by eq. (2.49) and $\Gamma_{\text{mag}} \equiv \tau_{\text{mag}}^{-1}$ is the bandwidth of magnon, and we used the rotating wave approximation. The last term of eq. (A.2) describes the mixing of magnons and cavity modes, and the magnon field \hat{d} has been redefined in comparison to eq. (3.21) for later convenience. Equation (A.3) represents the measurement of the cavity mode, the loss of the cavity electromagnetic field, and the

magnon excitation by axions as interactions with three ports: the measurement port \hat{a}_m , the loss port \hat{a}_l , and the axion port \hat{a}_a , respectively. The coupling constant for the loss port κ_l is determined with the cavity quality factor Q as $\kappa_l = m_a/Q$.

In Heisenberg picture, the equations of motion for $\hat{c}(t)$, $\hat{d}(t)$, and $\hat{a}_j(\omega, t)$ are

$$\frac{d\hat{c}(t)}{dt} = -i\omega_L\hat{c}(t) + g_{\text{eff}}\hat{d}(t) + \sum_{j=m,l} \sqrt{\frac{\kappa_j}{2\pi}} \int d\omega \hat{a}_j(\omega), \quad (\text{A.5})$$

$$\frac{d\hat{d}(t)}{dt} = -i\omega_L\hat{d}(t) - g_{\text{eff}}\hat{c}(t) - \frac{\Gamma_{\text{mag}}}{2}\hat{d}(t) + \sqrt{\frac{\kappa_a}{2\pi}} \int d\omega \hat{a}_a(\omega), \quad (\text{A.6})$$

$$\frac{d\hat{a}_j(\omega, t)}{dt} = -i\omega\hat{a}_j(\omega, t) - \sqrt{\frac{\kappa_j}{2\pi}} \begin{cases} \hat{c}(t) & (j = m, l) \\ \hat{d}(t) & (j = a) \end{cases}. \quad (\text{A.7})$$

The formal solution of eq. (A.7) is written with an initial time $t_{\text{in}} (< t)$ as

$$\hat{a}_j(\omega, t) = e^{-i\omega(t-t_{\text{in}})}\hat{a}_j(\omega, t_{\text{in}}) - \sqrt{\frac{\kappa_j}{2\pi}} \int_{t_{\text{in}}}^t dt' e^{-i\omega(t-t')} \begin{cases} \hat{c}(t') & (j = m, l) \\ \hat{d}(t') & (j = a) \end{cases}. \quad (\text{A.8})$$

Substituting eq. (A.8) into eqs. (A.5) and (A.6), we get the Heisenberg–Langevin equations,

$$\frac{d\hat{c}(t)}{dt} = -i\omega_L\hat{c}(t) - \frac{\kappa_c}{2}\hat{c}(t) + g_{\text{eff}}\hat{d}(t) + \sum_{j=m,l} \sqrt{\frac{\kappa_j}{2\pi}} \int d\omega e^{-i\omega(t-t_{\text{in}})}\hat{a}_j(\omega, t_{\text{in}}), \quad (\text{A.9})$$

$$\frac{d\hat{d}(t)}{dt} = -i\omega_L\hat{d}(t) - \frac{\kappa_d}{2}\hat{d}(t) - g_{\text{eff}}\hat{c}(t) + \sqrt{\frac{\kappa_a}{2\pi}} \int d\omega e^{-i\omega(t-t_{\text{in}})}\hat{a}_j(\omega, t_{\text{in}}), \quad (\text{A.10})$$

where $\kappa_c \equiv \kappa_m + \kappa_l$ and $\kappa_d \equiv \kappa_a + \Gamma_{\text{mag}}$. We define the so-called input field as

$$\hat{a}_{s,j}(t) \equiv \frac{1}{\sqrt{2\pi}} \int d\omega e^{-i\omega(t-t_{\text{in}})}\hat{a}_j(\omega, t_{\text{in}}). \quad (\text{A.11})$$

The input field of the measurement port is shown in fig. 3. In terms of the input fields, eqs. (A.9) and (A.10) are rewritten as

$$\frac{d\hat{c}(t)}{dt} = -i\omega_L\hat{c}(t) - \frac{\kappa_c}{2}\hat{c}(t) + g_{\text{eff}}\hat{d}(t) + \sum_{j=m,l} \sqrt{\kappa_j}\hat{a}_{s,j}(t), \quad (\text{A.12})$$

$$\frac{d\hat{d}(t)}{dt} = -i\omega_L\hat{d}(t) - \frac{\kappa_d}{2}\hat{d}(t) - g_{\text{eff}}\hat{c}(t) + \sqrt{\kappa_a}\hat{a}_{s,a}(t). \quad (\text{A.13})$$

We can formally solve eq. (A.7) with another time $t_{\text{out}} (> t > t_{\text{in}})$ as

$$\hat{a}_j(\omega, t) = e^{-i\omega(t-t_{\text{out}})}\hat{a}_j(\omega, t_{\text{out}}) - \sqrt{\frac{\kappa_j}{2\pi}} \int_{t_{\text{out}}}^t dt' e^{-i\omega(t-t')} \begin{cases} \hat{c}(t') & (j = m, l) \\ \hat{d}(t') & (j = a) \end{cases}, \quad (\text{A.14})$$

and we can also define the output field as

$$\hat{a}_{o,j}(t) \equiv \frac{1}{\sqrt{2\pi}} \int d\omega e^{-i\omega(t-t_{\text{out}})}\hat{a}_j(\omega, t_{\text{out}}). \quad (\text{A.15})$$

Noting that the right-hand sides of eqs. (A.8) and (A.14) have the same form, we find the input-output relation by integrating them by ω :

$$\hat{a}_{o,j}(t) = \hat{a}_{s,j}(t) - \sqrt{\kappa_j} \begin{cases} \hat{c}(t) & (j = m, l) \\ \hat{d}(t) & (j = a) \end{cases}. \quad (\text{A.16})$$

The output field of the measurement port is also shown in fig. 3. Transforming into the rotating frame, i.e., $\hat{A}(t) \rightarrow \hat{A}(t)e^{-i\omega_L t}$ for all annihilation operators, we can eliminate the first terms in eqs. (A.12) and (A.13). Thus, in the Fourier domain, we can solve eq. (A.13) as

$$\hat{d}(\Delta\omega) = \frac{1}{\kappa_d/2 - i\Delta\omega} [-g_{\text{eff}}\hat{c}(\omega) + \sqrt{\kappa_a}\hat{a}_{s,a}(\Delta\omega)], \quad (\text{A.17})$$

where $\Delta\omega \equiv \omega - \omega_L$. Substituting this into eq. (A.12) and using the input-output relation for the measurement port, we get

$$\hat{a}_{o,m}(\Delta\omega) = \sum_{j=m,l,a} \chi_j(\Delta\omega)\hat{a}_{s,j}(\Delta\omega), \quad (\text{A.18})$$

where

$$\chi_j(\Delta\omega) = \delta_{mj} - \left(\frac{\kappa_c}{2} + \frac{g_{\text{eff}}^2}{\kappa_d/2 - i\Delta\omega} - i\Delta\omega \right)^{-1} \times \sqrt{\kappa_m\kappa_j} \begin{cases} 1 & (j = m, l) \\ \frac{g_{\text{eff}}}{\kappa_d/2 - i\Delta\omega} & (j = a) \end{cases}. \quad (\text{A.19})$$

Note that the susceptibility $\chi_j(\Delta\omega)$ satisfies $\chi_j^*(-\Delta\omega) = \chi_j(\Delta\omega)$.

We move to the quadrature basis by

$$\begin{pmatrix} \hat{X}(\Delta\omega) \\ \hat{Y}(\Delta\omega) \end{pmatrix} = \frac{1}{\sqrt{2}} \begin{pmatrix} 1 & 1 \\ -i & i \end{pmatrix} \begin{pmatrix} \hat{a}(\Delta\omega) \\ \hat{a}^\dagger(-\Delta\omega) \end{pmatrix} \equiv \mathbf{P} \begin{pmatrix} \hat{a}(\Delta\omega) \\ \hat{a}^\dagger(-\Delta\omega) \end{pmatrix}. \quad (\text{A.20})$$

We would like to relate the output operator $\hat{X}_{\text{out},m}$, which goes out from the AMP JPA, with the input operator $\hat{X}_{\text{in},m}$, which comes into the SQ JPA, by an SSR/cavity susceptibility Ξ_j as $\hat{X}_{\text{out},m} = \sum_j \Xi_j \hat{X}_{\text{in},j}$. First, the SQ JPA squeezes $\hat{X}_{\text{in},m}$:

$$\vec{\hat{X}}_{s,m}(\Delta\omega) = \frac{1}{\sqrt{G_s}} \vec{\hat{X}}_{\text{in},m}(\Delta\omega), \quad (\text{A.21})$$

while leaving the operators at other ports unaffected. The SQ JPA amplifies the other quadrature at the measurement port $\hat{Y}_{\text{in},m}$ by $\sqrt{G_s}$, but we do not track the \hat{Y} quadratures because we will only measure the \hat{X} quadrature. Using eq. (A.18), we find that the susceptibility in the quadrature basis is the same as that in the original basis $\chi_j(\Delta\omega)$:

$$\begin{aligned} \begin{pmatrix} \hat{X}_{o,m}(\Delta\omega) \\ \hat{Y}_{o,m}(\Delta\omega) \end{pmatrix} &= \mathbf{P} \begin{pmatrix} \sum_j \chi_j(\Delta\omega) & 0 \\ 0 & \sum_j \chi_j^*(-\Delta\omega) \end{pmatrix} \mathbf{P}^{-1} \begin{pmatrix} \hat{X}_{s,j}(\Delta\omega) \\ \hat{Y}_{s,j}(\Delta\omega) \end{pmatrix} \\ &= \sum_j \begin{pmatrix} \chi_j(\Delta\omega) & 0 \\ 0 & \chi_j(\Delta\omega) \end{pmatrix} \begin{pmatrix} \hat{X}_{s,j}(\Delta\omega) \\ \hat{Y}_{s,j}(\Delta\omega) \end{pmatrix}. \end{aligned} \quad (\text{A.22})$$

Hence, $\hat{X}_{o,m}(\Delta\omega) = \sum_j \chi_j(\Delta\omega) \hat{X}_{s,j}(\Delta\omega)$. Finally, the AMP JPA performs amplification with a squeezing parameter G_a as

$$\hat{X}_{out,m}(\Delta\omega) = \sqrt{G_a} \hat{X}_{o,m}(\Delta\omega). \quad (\text{A.23})$$

As a result, we get the SSR/cavity susceptibility,

$$\Xi_j(\Delta\omega) = \begin{cases} \sqrt{\frac{G_a}{G_s}} \chi_j(\Delta\omega) & (j = m) \\ \sqrt{G_a} \chi_j(\Delta\omega) & (j = l, a) \end{cases}, \quad (\text{A.24})$$

and accordingly,

$$\begin{aligned} \hat{X}_{out,m}(\Delta\omega) &= \sum_{j=m,l,a} \Xi_j(\Delta\omega) \hat{X}_{in,j}(\Delta\omega) \\ &= \sqrt{G_a} \left[\frac{\chi_m(\Delta\omega)}{\sqrt{G_s}} \hat{X}_{in,m}(\Delta\omega) + \sum_{j=l,a} \chi_j(\Delta\omega) \hat{X}_{in,j}(\Delta\omega) \right]. \end{aligned} \quad (\text{A.25})$$

Next, we calculate the output power spectral density (PSD), $P(\Delta\omega)$. Equation (A.25) leads to

$$\begin{aligned} P(\Delta\omega) &\equiv \frac{1}{T_{\text{int}}} \left\langle \hat{X}_{out,m}^\dagger(\Delta\omega) \hat{X}_{out,m}(\Delta\omega) \right\rangle \\ &= \frac{G_a}{T_{\text{int}}} \left[\frac{|\chi_{mm}(\Delta\omega)|^2}{G_s} \left\langle \hat{X}_{in,m}^\dagger(\Delta\omega) \hat{X}_{in,m}(\Delta\omega) \right\rangle \right. \\ &\quad \left. + \sum_{j=l,a} |\chi_{mj}(\Delta\omega)|^2 \left\langle \hat{X}_{in,j}^\dagger(\Delta\omega) \hat{X}_{in,j}(\Delta\omega) \right\rangle \right], \end{aligned} \quad (\text{A.26})$$

where T_{int} is the integration time for each scan. The input spectral densities are

$$\frac{1}{T_{\text{int}}} \left\langle \hat{X}_{in,m}^\dagger(\Delta\omega) \hat{X}_{in,m}(\Delta\omega) \right\rangle = \frac{1}{T_{\text{int}}} \left\langle \hat{X}_{in,l}^\dagger(\Delta\omega) \hat{X}_{in,l}(\Delta\omega) \right\rangle = n_T + \frac{1}{2}, \quad (\text{A.27})$$

$$\frac{1}{T_{\text{int}}} \left\langle \hat{X}_{in,a}^\dagger(\Delta\omega) \hat{X}_{in,a}(\Delta\omega) \right\rangle = n_a + \frac{1}{2}, \quad (\text{A.28})$$

where n_T and n_a are the numbers of the input thermal photon and the axion per unit time per unit bandwidth, respectively. We assumed that the thermal noise dominates the input noise for the measurement port and the loss port. Note that n_T and $1/2$ s in the spectral density matrix correspond to the thermal and the quantum noises, respectively. We also assume $n_T \ll 1/2$ since our experiment is operated under a low temperature $T < T_c \simeq \mathcal{O}(1)$ mK, which is lower than the SQL temperature $T_{\text{SQL}} = m_a/k_B \sim \mathcal{O}(10)$ mK. Decomposing the PSD into the signal and the noise part, we get the signal and the noise

spectral densities $S(\Delta\omega)$ and $B(\Delta\omega)$,

$$S(\Delta\omega) = \frac{G_a}{T_{\text{int}}} \left| \frac{\kappa_c}{2} + \frac{g_{\text{eff}}^2}{\kappa_d/2 - i\Delta\omega} - i\Delta\omega \right|^{-2} \frac{g_{\text{eff}}^2 \kappa_m}{(\kappa_d/2)^2 + (\Delta\omega)^2} \kappa_a n_a, \quad (\text{A.29})$$

$$B(\Delta\omega) = \frac{G_a}{2T_{\text{int}}} \left| \frac{\kappa_c}{2} + \frac{g_{\text{eff}}^2}{\kappa_d/2 - i\Delta\omega} - i\Delta\omega \right|^{-2} \times \left[\frac{1}{G_s} \left\{ \left(\frac{-\kappa_m + \kappa_l}{2} + \frac{g_{\text{eff}}^2}{(\kappa_d/2)^2 + (\Delta\omega)^2} \frac{\kappa_d}{2} \right)^2 + \left(\frac{g_{\text{eff}}^2}{(\kappa_d/2)^2 + (\Delta\omega)^2} - 1 \right)^2 (\Delta\omega)^2 \right\} + \kappa_m \kappa_l + \frac{g_{\text{eff}}^2 \kappa_m \kappa_a}{(\kappa_d/2)^2 + (\Delta\omega)^2} \right]. \quad (\text{A.30})$$

A.2 Creation Rate of Magnons

Let us compute the creation rate of magnons in order to estimate $\kappa_a n_a$. We start with the equation of motion for the magnon operator,

$$\frac{d\hat{d}(t)}{dt} = -i\omega_L \hat{d}(t) - \frac{\Gamma_{\text{mag}}}{2} \hat{d}(t) - i \frac{C_{\text{ann}}}{f_a} \sqrt{\rho_a N} v_a^+(t) \sin[\omega_L t + \varphi(t)], \quad (\text{A.31})$$

where the last term comes from the axion-magnon interaction derived in eq. (3.8). Under the assumption $\hat{d}(0) = 0$, the formal solution is

$$\hat{d}(t) = -i \frac{C_{\text{ann}}}{f_a} \sqrt{\rho_a N} \int_0^t dt' e^{(-i\omega_L - \Gamma_{\text{mag}}/2)(t-t')} v_a^+(t') \sin[\omega_L t' + \varphi(t')]. \quad (\text{A.32})$$

It is convenient to introduce the autocorrelation function $C(t, t') \equiv \langle \hat{d}^\dagger(t) \hat{d}(t') \rangle$, where the expectation value is taken for the stochastic values: the axion velocity $v_a(t)$ and the phase $\varphi(t)$. For $t, t' \gg \tau_a$, where τ_a is the axion coherence time $\tau_a \simeq (m_a v_a^2)^{-1}$, we can compute $C(t, t')$ as

$$\begin{aligned} C(t, t') &= \left(\frac{C_{\text{ann}}}{f_a} \right)^2 \rho_a N \int_0^t d\bar{t} \int_0^{t'} d\bar{t}' e^{(+i\omega_L - \Gamma_{\text{mag}}/2)(t-\bar{t})} e^{(-i\omega_L - \Gamma_{\text{mag}}/2)(t'-\bar{t}')} \\ &\quad \times \langle v_a^-(\bar{t}) v_a^+(\bar{t}') \sin[\omega_L \bar{t} + \varphi(\bar{t})] \sin[\omega_L \bar{t}' + \varphi(\bar{t}')] \rangle \\ &\simeq \left(\frac{C_{\text{ann}}}{f_a} \right)^2 \rho_a N \int_0^t d\bar{t} \int_0^{t'} d\bar{t}' e^{(+i\omega_L - \Gamma_{\text{mag}}/2)(t-\bar{t})} e^{(-i\omega_L - \Gamma_{\text{mag}}/2)(t'-\bar{t}')} \\ &\quad \times \frac{1}{3} v_a^2 \cos[\omega_L(\bar{t} - \bar{t}')] \Theta(\tau_a - |\bar{t} - \bar{t}'|) \\ &\simeq \frac{2}{3} \left(\frac{C_{\text{ann}}}{f_a} \right)^2 \rho_a N v_a^2 \tau_a e^{i\omega_L(t-t')} e^{-(\Gamma_{\text{mag}}/2)(t+t')} \Gamma_{\text{mag}}^{-1} \left[e^{\Gamma_{\text{mag}} \min[t, t']} - 1 \right]. \end{aligned} \quad (\text{A.33})$$

In order to get the second line, we used an assumption that stochastic quantities do not correlate unless $|\bar{t} - \bar{t}'| < \tau_a$. The spectral density is obtained by Fourier-transforming $C(t, t')$,

$$\begin{aligned} \frac{1}{T_{\text{int}}} \langle \hat{d}^\dagger(\omega) \hat{d}(\omega) \rangle &= \frac{1}{T_{\text{int}}} \int_0^{T_{\text{int}}} dt \int_0^{T_{\text{int}}} dt' e^{-i\omega(t-t')} C(t, t') \\ &\simeq \frac{8}{3} \left(\frac{C_{\text{ann}}}{f_a} \right)^2 \rho_a N v_a^2 \tau_a \frac{1}{\Gamma_{\text{mag}}^2 + 4\Delta\omega^2}. \end{aligned} \quad (\text{A.34})$$

Here, we used $T_{\text{int}} \gg \Gamma_{\text{mag}}^{-1}$.

Next, we will estimate $\kappa_a n_a$. The solution of eq. (A.13) in the Fourier domain with $\hat{c} = 0$ leads to

$$\hat{a}_{s,a}(\Delta\omega) = \frac{\kappa_d/2 - i\Delta\omega}{\sqrt{\kappa_a}} \hat{d}^\dagger(\Delta\omega) \simeq \frac{\Gamma_{\text{mag}}/2 - i\Delta\omega}{\sqrt{\kappa_a}} \hat{d}^\dagger(\Delta\omega), \quad (\text{A.35})$$

where we assumed $\kappa_a \ll \Gamma_{\text{mag}}$. Thus, n_a is estimated as

$$\begin{aligned} n_a &= \frac{1}{T_{\text{int}}} \left\langle \hat{a}_{\text{in},a}^\dagger(\Delta\omega) \hat{a}_{\text{in},a}(\Delta\omega) \right\rangle \\ &\simeq \frac{(\Gamma_{\text{mag}}/2)^2 + \Delta\omega^2}{\kappa_a} \frac{1}{T_{\text{int}}} \left\langle \hat{d}^\dagger(\Delta\omega) \hat{d}(\Delta\omega) \right\rangle \\ &= \frac{2}{3\kappa_a} \left(\frac{C_{\text{ann}}}{f_a} \right)^2 \rho_a N v_a^2 \tau_a, \end{aligned} \quad (\text{A.36})$$

and hence,

$$\kappa_a n_a \simeq \frac{2}{3} \left(\frac{C_{\text{ann}}}{f_a} \right)^2 \rho_a N v_a^2 \tau_a. \quad (\text{A.37})$$

Considering that n_a has a bandwidth $\Delta_a \simeq m_a v_a^2$, which was neglected in eq. (A.34) because $\Delta_a \gg \Gamma_{\text{mag}}$, we should modify eq. (A.37) as

$$\kappa_a n_a \simeq \frac{2}{3} \left(\frac{C_{\text{ann}}}{f_a} \right)^2 \rho_a N v_a^2 \tau_a \Theta(\Delta_a/2 - |\Delta\omega|). \quad (\text{A.38})$$

A.3 Test Statistic

In order to determine the 95% exclusion limit, we introduce a log-likelihood ratio test statistic q [34, 90]. It is computed in the limits of $T_{\text{int}} \gg \tau_{\text{mag}}, \tau_a$ and $S(\Delta\omega) \ll B(\Delta\omega)$ as

$$q = -\frac{T_{\text{int}}}{2\pi} \int_0^\infty d\omega \left(\frac{S(\Delta\omega)}{B(\Delta\omega)} \right)^2. \quad (\text{A.39})$$

When we assume $\kappa_a \ll \kappa_l \ll \{g_{\text{eff}}, \Gamma_{\text{mag}}, \kappa_m\}$, we can approximate q as

$$\begin{aligned} q &\simeq -\frac{8g_{\text{eff}}^4 \kappa_m^2 N^2 g_{\text{ann}}^4 \rho_a^2 v_a^4 \tau_a^2 T_{\text{int}}}{9\pi m_n^4} G_s^2 \\ &\quad \times \int_{-\Delta_a/2}^{\Delta_a/2} d(\Delta\omega) \left[(\Delta\omega)^4 + \left\{ \left(\frac{\kappa_m}{2} \right)^2 + \left(\frac{\Gamma_{\text{mag}}}{2} \right)^2 - 2g_{\text{eff}}^2 + G_s \kappa_m \kappa_l \right\} (\Delta\omega)^2 \right. \\ &\quad \left. + \left(\frac{\kappa_m}{2} \frac{\Gamma_{\text{mag}}}{2} - g_{\text{eff}}^2 \right)^2 + G_s \kappa_m \kappa_l \left(\frac{\Gamma_{\text{mag}}}{2} \right)^2 \right]^{-2}. \end{aligned} \quad (\text{A.40})$$

The 95% exclusion limit corresponds to the point $q \simeq -2.71$.

The parameter κ_m determines the speed of the signal readout, and we can choose the optimal coupling κ_m so that the size of the test statistic $|q|$ is maximized. For this purpose,

we maximize the following integral,

$$\begin{aligned}
I(\kappa_m) &= \kappa_m^2 \int_{-\Delta_a/2}^{\Delta_a/2} d(\Delta\omega) \left[(\Delta\omega)^4 + \left\{ \left(\frac{\kappa_m}{2} \right)^2 + \left(\frac{\Gamma_{\text{mag}}}{2} \right)^2 - 2g_{\text{eff}}^2 + G_s \kappa_m \kappa_l \right\} (\Delta\omega)^2 \right. \\
&\quad \left. + \left(\frac{\kappa_m \Gamma_{\text{mag}}}{2} - g_{\text{eff}}^2 \right)^2 + G_s \kappa_m \kappa_l \left(\frac{\Gamma_{\text{mag}}}{2} \right)^2 \right]^{-2} \\
&\equiv \kappa_m^2 \int_{-\Delta_a/2}^{\Delta_a/2} d(\Delta\omega) \frac{1}{[\Delta\omega^4 + \xi(\kappa_m)\Delta\omega^2 + \zeta(\kappa_m)]^2}. \tag{A.41}
\end{aligned}$$

The approximate width of the integrand is

$$\delta \equiv 2\sqrt{\frac{-|\xi| + \sqrt{\xi^2 + 4\zeta}}{2}} = \begin{cases} 2\zeta^{1/4} & \text{for } \xi^2 \ll \zeta \\ 2\sqrt{\zeta/|\xi|} & \text{for } \xi^2 \gg \zeta \end{cases}, \tag{A.42}$$

which is equal to the full width at half maximum of the integrand when $\xi > 0$. As ξ increases, the peak width of the integrand narrows but the height remains the same. On the other hand, as ζ decreases, the peak becomes narrower and higher. We discuss the maximization of $I(\kappa_m)$ in two cases: $\delta \ll \Delta_a$ and $\delta \gg \Delta_a$.

In what follows, we will fix the value of g_{eff} as $g_{\text{eff}}/2\pi \equiv 0.3 \text{ MHz}$ for the purpose of order estimation, following eq. (3.24). Note that the precise value of g_{eff} highly depends on the shape of the cavity and thus should be evaluated after fixing the experimental setups.

Case 1. $\delta \ll \Delta_a$

It is necessary to fine-tune κ_m to $\kappa_m^* \simeq 4g_{\text{eff}}^2/\Gamma_{\text{mag}}$ in order to have $\delta \ll \Delta_a$. With this optimal coupling, ξ and ζ become

$$\begin{aligned}
\xi(\kappa_m^*) &= \left(\frac{\Gamma_{\text{mag}}}{2} \right)^2 \left[\left(\frac{2g_{\text{eff}}}{\Gamma_{\text{mag}}} \right)^2 - 1 \right]^2 + 4G_s \kappa_l \frac{g_{\text{eff}}^2}{\Gamma_{\text{mag}}} \\
&\simeq 6.5 \times 10^1 \text{ MHz}^2 + 2.6 \times 10^4 \text{ MHz}^2 \left(\frac{G_s}{Q} \right) \left(\frac{m_a}{1 \mu\text{eV}} \right), \tag{A.43}
\end{aligned}$$

$$\begin{aligned}
\zeta(\kappa_m^*) &= G_s \kappa_l g_{\text{eff}}^2 \Gamma_{\text{mag}} \\
&\simeq 4.4 \times 10^3 \text{ MHz}^4 \left(\frac{G_s}{Q} \right) \left(\frac{m_a}{1 \mu\text{eV}} \right). \tag{A.44}
\end{aligned}$$

If $Q/G_s \gtrsim 4 \times 10^3$, the first term in eq. (A.43) dominates ξ , while if $Q/G_s \lesssim 4 \times 10^3$, the second term in eq. (A.43) dominates ξ . Thus, δ reads

$$\begin{aligned}
\delta &= 2\sqrt{\zeta/\xi} \\
&\simeq \begin{cases} 4\sqrt{\frac{G_s \kappa_l}{\Gamma_{\text{mag}}} g_{\text{eff}} \left| \left(\frac{2g_{\text{eff}}}{\Gamma_{\text{mag}}} \right)^2 - 1 \right|^{-1}} \\ \simeq 1.6 \times 10^1 \text{ MHz} \left(\frac{G_s}{Q} \right)^{1/2} \left(\frac{m_a}{1 \mu\text{eV}} \right)^{1/2} & \text{for } Q/G_s \gtrsim 4 \times 10^3 \\ \Gamma_{\text{mag}} \simeq 8.3 \times 10^{-1} \text{ MHz} & \text{for } Q/G_s \lesssim 4 \times 10^3 \end{cases}. \tag{A.45}
\end{aligned}$$

In order to achieve $\delta \ll \Delta_a$ where

$$\Delta_a \simeq m_a v_a^2 \simeq 1.5 \text{ kHz} \left(\frac{m_a}{1 \mu\text{eV}} \right), \quad (\text{A.46})$$

we further need to take $Q/G_s \gtrsim 1.1 \times 10^8$. Under this condition, $I(\kappa_m^*)$ is calculated as

$$\begin{aligned} I(\kappa_m^*) &\simeq (\kappa_m^*)^2 \int_{-\infty}^{\infty} d(\Delta\omega) \frac{1}{[\Delta\omega^4 + \xi(\kappa_m^*)\Delta\omega^2 + \zeta(\kappa_m^*)]^2} \\ &= (\kappa_m^*)^2 \frac{\pi}{2\sqrt{\xi(\kappa_m^*)\zeta(\kappa_m^*)^3}}. \end{aligned} \quad (\text{A.47})$$

Therefore, we get

$$\begin{aligned} q &\simeq -\frac{8g_{\text{eff}}^4 N^2 g_{\text{ann}}^4 \rho_a^2 v_a^4 \tau_a^2 T_{\text{int}}}{9\pi m_n^4} G_s^2 \cdot 16 \frac{g_{\text{eff}}^4}{\Gamma_{\text{mag}}^2} \frac{\pi}{2} \frac{2}{\Gamma_{\text{mag}}} \left| \left(\frac{2g_{\text{eff}}}{\Gamma_{\text{mag}}} \right)^2 - 1 \right|^{-1} (G_s \kappa_l g_{\text{eff}}^2 \Gamma_{\text{mag}})^{-3/2} \\ &= -\frac{128g_{\text{eff}}^5 N^2 g_{\text{ann}}^4 \rho_a^2 T_{\text{int}} G_s^{1/2} Q^{3/2}}{9m_n^4 \Gamma_{\text{mag}}^{9/2} m_a^{7/2}} \left| \left(\frac{2g_{\text{eff}}}{\Gamma_{\text{mag}}} \right)^2 - 1 \right|^{-1} \\ &\simeq -6.9 \times 10^{58} g_{\text{ann}}^4 \left(\frac{T_{\text{int}}}{1 \text{ day}} \right) \left(\frac{m_a}{1 \mu\text{eV}} \right)^{-7/2} \left(\frac{G_s}{10^2} \right)^{1/2} \left(\frac{M}{100 \text{ g}} \right)^2 \left(\frac{Q}{10^{11}} \right)^{3/2}. \end{aligned} \quad (\text{A.48})$$

Case 2. $\delta \gg \Delta_a$

When $Q/G_s \lesssim 1.1 \times 10^8$, we have $\delta \gg \Delta_a$, and thus $I(\kappa_m)$ reads

$$I(\kappa_m) \simeq \kappa_m^2 \frac{\Delta_a}{\zeta(\kappa_m)^2}. \quad (\text{A.49})$$

This is maximized by taking the optimal coupling $\kappa_m = \kappa_m^* = 4g_{\text{eff}}^2/\Gamma_{\text{mag}}$. Then q becomes

$$\begin{aligned} q &= -\frac{8g_{\text{eff}}^4 N^2 g_{\text{ann}}^4 \rho_a^2 v_a^4 \tau_a^2 T_{\text{int}}}{9\pi m_n^4} \Delta_a \left[\kappa_l \left(\frac{\Gamma_{\text{mag}}}{2} \right)^2 \right]^{-2} \\ &= -\frac{128g_{\text{eff}}^4 N^2 g_{\text{ann}}^4 \rho_a^2 v_a^2 T_{\text{int}} Q^2}{9\pi m_n^4 \Gamma_{\text{mag}}^4 m_a^3} \\ &\simeq -2.5 \times 10^{49} g_{\text{ann}}^4 \left(\frac{T_{\text{int}}}{1 \text{ day}} \right) \left(\frac{m_a}{1 \mu\text{eV}} \right)^{-3} \left(\frac{G_s}{10^2} \right)^0 \left(\frac{M}{100 \text{ g}} \right)^2 \left(\frac{Q}{10^6} \right)^2. \end{aligned} \quad (\text{A.50})$$

One can see that the sensitivity cannot be improved by squeezing since q does not depend on G_s in this case.

B Josephson parametric amplifier (JPA)

Here, we will review about Josephson parametric amplifier (JPA).

B.1 Effective description

Let us imagine that the circuit model has two junctions at x_1 and x_2 . The effective Hamiltonian is given by

$$H = \int d^3x \left[\frac{1}{2m} |\vec{D}\Psi_1|^2 + V(\Psi_1) + \frac{1}{2m} |\vec{D}\Psi_2|^2 + V(\Psi_2) \right] \quad (\text{B.1})$$

$$+ \alpha \Psi_2^* \Psi_1 [\delta(x - x_1) + \delta(x - x_2)] + \text{h.c.}, \quad (\text{B.2})$$

where x_1, x_2 represent the places of the junctions, and Ψ_1, Ψ_2 are the wave functions of Cooper pairs, where $\Psi_1(x)$ lives within the interval $x_1 < x < x_2$, while $\Psi_2(x)$ within $x_2 < x < x_1$ (note that this is a loop). In the case of a circuit without any junctions, energy minimization requires

$$\vec{0} = \vec{D}\Psi = \vec{\nabla}\Psi - i2e\vec{A}\Psi = i|\Psi|(\vec{\nabla}\theta - 2e\vec{A}), \quad (\text{B.3})$$

where θ is the phase of Ψ and \vec{A} is the photon field. Integrating along the circuit, we get

$$2\pi n = \oint \vec{\nabla}\theta = \oint 2e\vec{A} = 2e\Phi, \quad (\text{B.4})$$

with an integer n . We used the single-valuedness of the wave function for the left equation, and Φ is the magnetic flux. For the Josephson junction, however, $\vec{\nabla}\theta_{1,2}$ need to be treated independently and hence the magnetic flux does not need to be quantized,

$$2e\Phi = \oint \vec{\nabla}\theta = \int_{x_1}^{x_2} \vec{\nabla}\theta_1 + \int_{x_2}^{x_1} \vec{\nabla}\theta_2 = \theta_1(x_2) - \theta_1(x_1) + \theta_2(x_1) - \theta_2(x_2). \quad (\text{B.5})$$

For our purposes, we are not interested in the dynamics in the bulk of the superconductor where all excitations are gapped but rather only in the junctions where the phase degrees of freedom can have much smaller excitation energies. Noting the canonical commutation relation

$$[\Psi(x), \Psi^\dagger(y)] = \delta(x - y), \quad (\text{B.6})$$

and rewriting it as $\Psi(x) = \sqrt{N(x)}e^{i\theta(x)}$, we can derive⁵

$$[\theta(x), N(y)] = i\delta(x - y). \quad (\text{B.7})$$

In addition, we are only interested in the phase differences across the junction. Therefore we reduce the degrees of freedom down to $\vartheta_1 = \theta_2(x_1) - \theta_1(x_1)$ and $\vartheta_2 = \theta_1(x_2) - \theta_2(x_2)$ subject to the constraint $\vartheta_1 + \vartheta_2 = 2e\Phi$.

On the other hand, across the junctions we expect a capacitance C so that the Hamiltonian contains

$$\frac{Q(x_{1,2})^2}{2C} = \frac{(2e)^2}{2C} n_{1,2}^2, \quad (\text{B.8})$$

⁵Considering the periodicity of θ , the right commutation relation of these variables is

$$[e^{i\theta(x)}, N(y)] = e^{i\theta(x)}\delta(x - y).$$

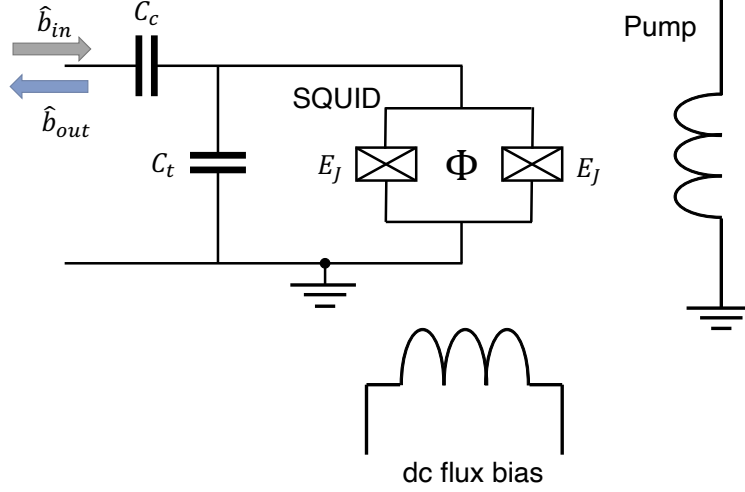


Figure 6. Schematic of a flux-driven Josephson parametric amplifier (FJPA). It consists of a SQUID biased by the external flux $\Phi_{\text{ext}} = \Phi_{\text{DC}} + \Phi_{\text{AC}} \cos(\alpha\omega_c t)$ and a shunting capacitance C_t , and is connected to the input/output port. We assume two junctions in the SQUID have the same Josephson energies E_J .

where we defined $n_1 = \frac{1}{2}N_2(x_1) - \frac{1}{2}N_1(x_1)$ and $n_2 = \frac{1}{2}N_1(x_2) - \frac{1}{2}N_2(x_2)$. Here we made a simplification that the capacitance is the same for both junctions. Combining them together, we find the simplified Hamiltonian

$$H = \frac{2e^2}{C}(n_1^2 + n_2^2) + 2\alpha(\sqrt{N_1(x_1)N_2(x_1)} \cos \vartheta_1 + \sqrt{N_1(x_2)N_2(x_2)} \cos \vartheta_2). \quad (\text{B.9})$$

We define $\vartheta \equiv (\vartheta_1 - \vartheta_2)/2$ and its canonical conjugate $n = n_1 - n_2$. Assuming that two Josephson energies are same, $2\alpha\sqrt{N_1(x_1)N_2(x_1)} = 2\alpha\sqrt{N_1(x_2)N_2(x_2)} = -E_J$, we get

$$H = \frac{e^2}{C}n^2 - 2E_J \cos(e\Phi) \cos(\vartheta). \quad (\text{B.10})$$

Here we neglected the term proportional to $(n_1 + n_2)^2$ since the value of $n_1 + n_2$ is conserved.

B.2 Flux-driven Josephson parametric amplifier

In the following, we explain how the flux-driven Josephson parametric amplifiers (FJPA) work in squeezing and amplifying the signal. We consider the simplified theoretical model of the FJPA (fig. 6). The FJPA consists of a SQUID biased by the external flux Φ_{ext} and a shunting capacitance C_t and is connected to the input/output port.

Similarly to eq. (B.10), The Hamiltonian describing the resonator part of FJPA is

$$\begin{aligned} H_{\text{sys}} &= \frac{(2en)^2}{2C_t} - E_J \cos \vartheta_1 - E_J \cos \vartheta_2 \\ &= 4E_C n^2 - E_J^{\text{eff}}(\Phi_{\text{ext}}) \cos \vartheta, \end{aligned} \quad (\text{B.11})$$

where $E_C = e^2/(2C_t)$, $E_J^{\text{eff}}(\Phi_{\text{ext}}) = 2E_J \cos(e\Phi_{\text{ext}}) = 2E_J \cos(\pi\Phi_{\text{ext}}/\Phi_0)$. We set the DC part of Φ_{ext} to the quarter of magnetic flux quantum, i.e., bias the amplifier at $\Phi_{\text{DC}} = \Phi_0/4$.

In the absence of a pump,

$$H_{\text{sys}} = 4E_C n^2 - \sqrt{2}E_J \cos \vartheta. \quad (\text{B.12})$$

Expanding $\cos \vartheta$ to order ϑ^2 , we can write the Hamiltonian by the ladder operator.

$$H_{\text{sys}} = \omega_c \hat{a}^\dagger \hat{a}, \quad (\text{B.13})$$

where

$$\vartheta = \left(\frac{\sqrt{2}E_C}{E_J} \right)^{1/4} (\hat{a}^\dagger + \hat{a}), \quad (\text{B.14})$$

$$n = \frac{i}{2} \left(\frac{E_J}{\sqrt{2}E_C} \right)^{1/4} (\hat{a}^\dagger - \hat{a}), \quad (\text{B.15})$$

$$\omega_c = 2\sqrt{2\sqrt{2}E_C E_J}. \quad (\text{B.16})$$

Next, we consider including the AC part of the external field Φ_{ext} due to the pumping

$$\Phi_{\text{ext}} = \Phi_{\text{DC}} + \Phi_{\text{AC}} \cos(\alpha\omega_c t). \quad (\text{B.17})$$

We set the AC part of Φ_{ext} smaller than the DC part $\Phi_{\text{AC}} \ll \Phi_{\text{DC}}$, and evaluate $E_J^{\text{eff}}(\Phi_{\text{ext}})$ as

$$\begin{aligned} E_J^{\text{eff}}(\Phi_{\text{ext}}) &\simeq E_J^{\text{eff}}(\Phi_{\text{DC}}) + \left. \frac{\partial E_J^{\text{eff}}(\Phi)}{\partial \Phi} \right|_{\Phi=\Phi_{\text{DC}}} \Phi_{\text{AC}} \cos(\alpha\omega_c t) \\ &= \sqrt{2}E_J - \left(\frac{\pi\Phi_{\text{AC}}}{\Phi_0} \right) \sqrt{2}E_J \cos(\alpha\omega_c t). \end{aligned} \quad (\text{B.18})$$

Thus, Hamiltonian H_{sys} becomes

$$H_{\text{sys}} \simeq \omega_c \hat{a}^\dagger \hat{a} + \mu_r \cos(\alpha\omega_c t) (\hat{a}^\dagger + \hat{a})^2, \quad (\text{B.19})$$

where $\mu_r = \frac{\pi\Phi_{\text{AC}}}{\Phi_0} \left(\frac{E_C E_J}{\sqrt{2}} \right)^{\frac{1}{2}}$. We focus on the parametric amplifier region ($\alpha \simeq 2$). Applying rotating wave approximation, we can estimate H_{sys} as

$$H_{\text{sys}} \simeq \omega_c \hat{a}^\dagger \hat{a} + \frac{\mu_r}{2} e^{i\alpha\omega_c t} \hat{a}^2 + \frac{\mu_r}{2} e^{-i\alpha\omega_c t} \hat{a}^{\dagger 2}. \quad (\text{B.20})$$

We assume the resonator has a semi-infinite waveguide mode (the annihilation operator of which is denoted as \hat{b}_k) connected as an input/output port and also has internal losses in the resonator (the annihilation operator of which is denoted as \hat{c}_k). The schematic of this parametric amplifier using opto-mechanical analogy is fig. 7. The total Hamiltonian describing this is

$$H_{\text{tot}} = H_{\text{sys}} + H_{\text{sig}} + H_{\text{loss}}, \quad (\text{B.21})$$

$$H_{\text{sys}} = \omega_c \hat{a}^\dagger \hat{a} + \frac{\mu_r}{2} e^{i\alpha\omega_c t} \hat{a}^2 + \frac{\mu_r}{2} e^{-i\alpha\omega_c t} \hat{a}^{\dagger 2}, \quad (\text{B.22})$$

$$H_{\text{sig}} = \int d\omega \left[\omega \hat{b}^\dagger(\omega) \hat{b}(\omega) + i\sqrt{\frac{\kappa_e}{2\pi}} (\hat{a}^\dagger \hat{b}(\omega) - \hat{b}^\dagger(\omega) \hat{a}) \right], \quad (\text{B.23})$$

$$H_{\text{loss}} = \int d\omega \left[\omega \hat{c}^\dagger(\omega) \hat{c}(\omega) + i\sqrt{\frac{\kappa_i}{2\pi}} (\hat{a}^\dagger \hat{c}(\omega) - \hat{c}^\dagger(\omega) \hat{a}) \right]. \quad (\text{B.24})$$

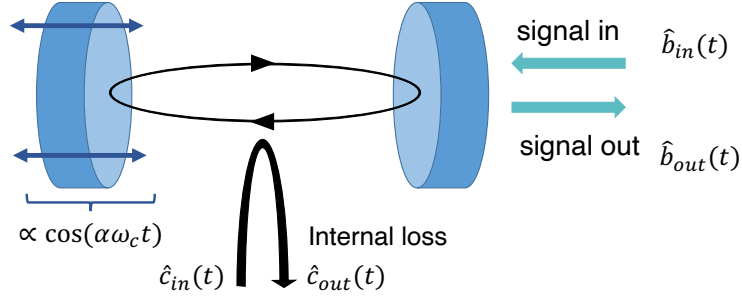


Figure 7. Schematic of the parametric amplifier. Here we use opto-mechanical analogy (resonator consisting of the cavity) instead of Josephson parametric amplifier.

Here, κ_e is the external loss rate of the resonator, and κ_i is the internal loss rate of the resonator. As we did in appendix A, we get Heisenberg equations for the resonator mode \hat{a} and the input-output relationship of the waveguide:

$$\frac{d\hat{a}(t)}{dt} = \left(-i\omega_c - \frac{\kappa}{2}\right) \hat{a}(t) - i\mu_r e^{-i\alpha\omega_c t} \hat{a}^\dagger(t) + \sqrt{\kappa_e} \hat{b}_{in}(t) + \sqrt{\kappa_i} \hat{c}_{in}(t), \quad (\text{B.25})$$

$$\hat{b}_{out}(t) = \hat{b}_{in}(t) - \sqrt{\kappa_e} \hat{a}(t), \quad (\text{B.26})$$

where $\kappa \equiv \kappa_i + \kappa_e$.

B.3 Resonator equation

In this subsection, we neglect the internal loss ($\kappa = \kappa_e$) and switch to a frame rotating at the angular frequency $\alpha\omega_c/2$, and define the following operators:

$$\hat{A}(t) = e^{i\frac{\alpha}{2}\omega_c t} \hat{a}(t), \quad (\text{B.27})$$

$$\hat{B}_{in(out)}(t) = e^{i\frac{\alpha}{2}\omega_c t} \hat{b}_{in(out)}(t). \quad (\text{B.28})$$

Assuming $\alpha = 2$ for simplicity, the resonator equation (B.25) and the input-output relation become

$$\begin{aligned} \frac{d\hat{A}(t)}{dt} &= -\frac{\kappa}{2} \hat{A}(t) - i\mu_r \hat{A}^\dagger(t) + \sqrt{\kappa} \hat{B}_{in}(t), \\ \hat{B}_{out}(t) &= \hat{B}_{in}(t) - \sqrt{\kappa} \hat{A}(t), \end{aligned} \quad (\text{B.29})$$

We consider the case with monochromatic incident light, i.e.,

$$\hat{B}_{in}(t) = \hat{B}_{in}(0) e^{-i\Delta\omega t}, \quad (\text{B.30})$$

where $\Delta\omega \equiv \omega - \omega_c$. In this case, the stationary solution of $\hat{A}(t)$ has only two Fourier components $e^{\pm i\Delta\omega t}$. The resonator equations for these components are

$$-i\Delta\omega \begin{pmatrix} \hat{A}(\Delta\omega) \\ \hat{A}^\dagger(-\Delta\omega) \end{pmatrix} = \begin{pmatrix} -\kappa/2 & -i\mu_r \\ +i\mu_r & -\kappa/2 \end{pmatrix} \begin{pmatrix} \hat{A}(\Delta\omega) \\ \hat{A}^\dagger(-\Delta\omega) \end{pmatrix} + \sqrt{\kappa} \begin{pmatrix} \hat{B}_{in}(0) \\ 0 \end{pmatrix}, \quad (\text{B.31})$$

and

$$+i\Delta\omega \begin{pmatrix} \hat{A}(-\Delta\omega) \\ \hat{A}^\dagger(\Delta\omega) \end{pmatrix} = \begin{pmatrix} -\kappa/2 & -i\mu_r \\ +i\mu_r & -\kappa/2 \end{pmatrix} \begin{pmatrix} \hat{A}(-\Delta\omega) \\ \hat{A}^\dagger(\Delta\omega) \end{pmatrix} + \sqrt{\kappa} \begin{pmatrix} 0 \\ \hat{B}_{\text{in}}^\dagger(0) \end{pmatrix}. \quad (\text{B.32})$$

Solving these equations, we obtain

$$\hat{A}(t) = \frac{\frac{\kappa}{2} - i\Delta\omega}{\left(\frac{\kappa}{2} - i\Delta\omega\right)^2 - \mu_r^2} \sqrt{\kappa} \hat{B}_{\text{in}}(0) e^{-i\Delta\omega t} + \frac{-i\mu_r}{\left(\frac{\kappa}{2} + i\Delta\omega\right)^2 - \mu_r^2} \sqrt{\kappa} \hat{B}_{\text{in}}^\dagger(0) e^{+i\Delta\omega t}. \quad (\text{B.33})$$

The output field is derived using eq. (B.29) as

$$\hat{B}_{\text{out}}(t) = \left[1 - \frac{\left(\frac{\kappa}{2} - i\Delta\omega\right)\kappa}{\left(\frac{\kappa}{2} - i\Delta\omega\right)^2 - \mu_r^2} \right] \hat{B}_{\text{in}}(0) e^{-i\Delta\omega t} + \frac{-i\mu_r\kappa}{\left(\frac{\kappa}{2} + i\Delta\omega\right)^2 - \mu_r^2} \hat{B}_{\text{in}}^\dagger(0) e^{+i\Delta\omega t}. \quad (\text{B.34})$$

The first term represents the signal component, and the second term represents the idler component.

When $\Delta\omega = 0$, these two modes degenerate. In this case, the output gain shows the phase-sensitivity. In order to verify this, we define the following quadratures:

$$\hat{X}_\theta \equiv \frac{\hat{B}e^{-i\theta} + \hat{B}^\dagger e^{i\theta}}{\sqrt{2}}, \quad (\text{B.35})$$

$$\hat{Y}_\theta \equiv \frac{\hat{B}e^{-i\theta} - \hat{B}^\dagger e^{i\theta}}{\sqrt{2}i}. \quad (\text{B.36})$$

From eq. (B.34) with $\Delta\omega = 0$, we find

$$\hat{X}_{\theta, \text{out}} = \left[1 - \frac{\frac{\kappa^2}{2}}{\frac{\kappa^2}{4} - \mu_r^2} - \frac{\mu_r\kappa \sin(2\theta)}{\frac{\kappa^2}{4} - \mu_r^2} \right] \hat{X}_{\theta, \text{in}} - \frac{\mu_r\kappa \cos(2\theta)}{\frac{\kappa^2}{4} - \mu_r^2} \hat{Y}_{\theta, \text{in}}, \quad (\text{B.37})$$

$$\hat{Y}_{\theta, \text{out}} = \left[1 - \frac{\frac{\kappa^2}{2}}{\frac{\kappa^2}{4} - \mu_r^2} + \frac{\mu_r\kappa \sin(2\theta)}{\frac{\kappa^2}{4} - \mu_r^2} \right] \hat{Y}_{\theta, \text{in}} - \frac{\mu_r\kappa \cos(2\theta)}{\frac{\kappa^2}{4} - \mu_r^2} \hat{X}_{\theta, \text{in}}. \quad (\text{B.38})$$

When $\theta = (1/4 + n)\pi$ ($n \in \mathbb{Z}$) in particular, they take the following form:

$$\hat{X}_{\theta, \text{out}} = \sqrt{G} \hat{X}_{\theta, \text{in}}, \quad \hat{Y}_{\theta, \text{out}} = \frac{1}{\sqrt{G}} \hat{Y}_{\theta, \text{in}}, \quad (\text{B.39})$$

where the parameter G is

$$G = \left(\frac{\mu_r + \frac{\kappa}{2}}{\mu_r - \frac{\kappa}{2}} \right)^2. \quad (\text{B.40})$$

Equation (B.39) represents the squeezing by a JPA and is what we used in eqs. (3.30) and (3.31).

References

- [1] R.D. Peccei and H.R. Quinn, *CP Conservation in the Presence of Instantons*, *Phys. Rev. Lett.* **38** (1977) 1440.
- [2] C. Abel et al., *Measurement of the Permanent Electric Dipole Moment of the Neutron*, *Phys. Rev. Lett.* **124** (2020) 081803 [[2001.11966](#)].
- [3] J. Preskill, M.B. Wise and F. Wilczek, *Cosmology of the Invisible Axion*, *Phys. Lett. B* **120** (1983) 127.
- [4] J.E. Kim, *Weak Interaction Singlet and Strong CP Invariance*, *Phys. Rev. Lett.* **43** (1979) 103.
- [5] M.A. Shifman, A.I. Vainshtein and V.I. Zakharov, *Can Confinement Ensure Natural CP Invariance of Strong Interactions?*, *Nucl. Phys. B* **166** (1980) 493.
- [6] M. Dine, W. Fischler and M. Srednicki, *A Simple Solution to the Strong CP Problem with a Harmless Axion*, *Phys. Lett. B* **104** (1981) 199.
- [7] A.R. Zhitnitsky, *On Possible Suppression of the Axion Hadron Interactions. (In Russian)*, *Sov. J. Nucl. Phys.* **31** (1980) 260.
- [8] S.J. Asztalos, G. Carosi, C. Hagmann, D. Kinion, K. Van Bibber, M. Hotz et al., *Squid-based microwave cavity search for dark-matter axions*, *Physical review letters* **104** (2010) 041301.
- [9] ADMX collaboration, *A Search for Invisible Axion Dark Matter with the Axion Dark Matter Experiment*, *Phys. Rev. Lett.* **120** (2018) 151301 [[1804.05750](#)].
- [10] ADMX collaboration, *Extended Search for the Invisible Axion with the Axion Dark Matter Experiment*, *Phys. Rev. Lett.* **124** (2020) 101303 [[1910.08638](#)].
- [11] ADMX collaboration, *Search for Invisible Axion Dark Matter in the 3.3–4.2 μeV Mass Range*, *Phys. Rev. Lett.* **127** (2021) 261803 [[2110.06096](#)].
- [12] HAYSTAC collaboration, *Results from phase 1 of the HAYSTAC microwave cavity axion experiment*, *Phys. Rev. D* **97** (2018) 092001 [[1803.03690](#)].
- [13] HAYSTAC collaboration, *A quantum-enhanced search for dark matter axions*, *Nature* **590** (2021) 238 [[2008.01853](#)].
- [14] HAYSTAC collaboration, *New results from HAYSTAC's phase II operation with a squeezed state receiver*, *Phys. Rev. D* **107** (2023) 072007 [[2301.09721](#)].
- [15] B.T. McAllister, G. Flower, J. Kruger, E.N. Ivanov, M. Goryachev, J. Bourhill et al., *The ORGAN Experiment: An axion haloscope above 15 GHz*, *Phys. Dark Univ.* **18** (2017) 67 [[1706.00209](#)].
- [16] A.P. Quiskamp, B.T. McAllister, P. Altin, E.N. Ivanov, M. Goryachev and M.E. Tobar, *Direct search for dark matter axions excluding ALPogenesis in the 63- to 67- μeV range with the ORGAN experiment*, *Sci. Adv.* **8** (2022) abq3765 [[2203.12152](#)].
- [17] D. Alesini et al., *Galactic axions search with a superconducting resonant cavity*, *Phys. Rev. D* **99** (2019) 101101 [[1903.06547](#)].
- [18] D. Alesini et al., *Search for invisible axion dark matter of mass $m_a = 43 \mu\text{eV}$ with the QUAX- $\alpha\gamma$ experiment*, *Phys. Rev. D* **103** (2021) 102004 [[2012.09498](#)].
- [19] D. Alesini et al., *Search for Galactic axions with a high-Q dielectric cavity*, *Phys. Rev. D* **106** (2022) 052007 [[2208.12670](#)].

- [20] S. Lee, S. Ahn, J. Choi, B.R. Ko and Y.K. Semertzidis, *Axion Dark Matter Search around $6.7 \mu\text{eV}$* , *Phys. Rev. Lett.* **124** (2020) 101802 [[2001.05102](#)].
- [21] J. Jeong, S. Youn, S. Bae, J. Kim, T. Seong, J.E. Kim et al., *Search for Invisible Axion Dark Matter with a Multiple-Cell Haloscope*, *Phys. Rev. Lett.* **125** (2020) 221302 [[2008.10141](#)].
- [22] CAPP collaboration, *First Results from an Axion Haloscope at CAPP around $10.7 \mu\text{eV}$* , *Phys. Rev. Lett.* **126** (2021) 191802 [[2012.10764](#)].
- [23] Y. Lee, B. Yang, H. Yoon, M. Ahn, H. Park, B. Min et al., *Searching for Invisible Axion Dark Matter with an 18 T Magnet Haloscope*, *Phys. Rev. Lett.* **128** (2022) 241805 [[2206.08845](#)].
- [24] J. Kim et al., *Near-Quantum-Noise Axion Dark Matter Search at CAPP around $9.5 \mu\text{eV}$* , *Phys. Rev. Lett.* **130** (2023) 091602 [[2207.13597](#)].
- [25] A.K. Yi et al., *Axion Dark Matter Search around $4.55 \mu\text{eV}$ with Dine-Fischler-Srednicki-Zhitnitskii Sensitivity*, *Phys. Rev. Lett.* **130** (2023) 071002 [[2210.10961](#)].
- [26] D.F. Jackson Kimball et al., *Overview of the Cosmic Axion Spin Precession Experiment (CASPEr)*, *Springer Proc. Phys.* **245** (2020) 105 [[1711.08999](#)].
- [27] T. Wu et al., *Search for Axionlike Dark Matter with a Liquid-State Nuclear Spin Comagnetometer*, *Phys. Rev. Lett.* **122** (2019) 191302 [[1901.10843](#)].
- [28] A. Garcon et al., *Constraints on bosonic dark matter from ultralow-field nuclear magnetic resonance*, *Sci. Adv.* **5** (2019) eaax4539 [[1902.04644](#)].
- [29] NASDUCK collaboration, *New constraints on axion-like dark matter using a Floquet quantum detector*, *Sci. Adv.* **8** (2022) abl8919 [[2105.04603](#)].
- [30] I.M. Bloch, Y. Hochberg, E. Kuflik and T. Volansky, *Axion-like Relics: New Constraints from Old Comagnetometer Data*, *JHEP* **01** (2020) 167 [[1907.03767](#)].
- [31] J. Lee, M. Lisanti, W.A. Terrano and M. Romalis, *Laboratory Constraints on the Neutron-Spin Coupling of feV -Scale Axions*, *Phys. Rev. X* **13** (2023) 011050 [[2209.03289](#)].
- [32] P.W. Graham, S. Hacıömeroğlu, D.E. Kaplan, Z. Omarov, S. Rajendran and Y.K. Semertzidis, *Storage ring probes of dark matter and dark energy*, *Phys. Rev. D* **103** (2021) 055010 [[2005.11867](#)].
- [33] C. Gao, W. Halperin, Y. Kahn, M. Nguyen, J. Schütte-Engel and J.W. Scott, *Axion Wind Detection with the Homogeneous Precession Domain of Superfluid Helium-3*, *Phys. Rev. Lett.* **129** (2022) 211801 [[2208.14454](#)].
- [34] J.A. Dror, S. Gori, J.M. Leedom and N.L. Rodd, *On the Sensitivity of Spin-Precession Axion Experiments*, [2210.06481](#).
- [35] C. Brandenstein, S. Stelzl, E. Gutsmedl, W. Schott, A. Weiler and P. Fierlinger, *Towards an electrostatic storage ring for fundamental physics measurements*, *EPJ Web Conf.* **282** (2023) 01017 [[2211.08439](#)].
- [36] K. Wei et al., *Dark matter search with a strongly-coupled hybrid spin system*, [2306.08039](#).
- [37] S. Chigusa, T. Moroi, K. Nakayama and T. Sichanugrist, *Dark matter detection using nuclear magnetization in magnet with hyperfine interaction*, [2307.08577](#).
- [38] C.M. Caves, *Quantum limits on noise in linear amplifiers*, *Physical Review D* **26** (1982) 1817.

- [39] M. Malnou, D.A. Palken, B.M. Brubaker, L.R. Vale, G.C. Hilton and K.W. Lehnert, *Squeezed vacuum used to accelerate the search for a weak classical signal*, *Phys. Rev. X* **9** (2019) 021023 [1809.06470].
- [40] K. Wurtz, B.M. Brubaker, Y. Jiang, E.P. Ruddy, D.A. Palken and K.W. Lehnert, *Cavity Entanglement and State Swapping to Accelerate the Search for Axion Dark Matter*, *PRX Quantum* **2** (2021) 040350 [2107.04147].
- [41] H. Zheng, M. Silveri, R.T. Brierley, S.M. Girvin and K.W. Lehnert, *Accelerating dark-matter axion searches with quantum measurement technology*, **1607.02529**.
- [42] T. Ikeda, A. Ito, K. Miuchi, J. Soda, H. Kurashige and Y. Shikano, *Axion search with quantum nondemolition detection of magnons*, *Phys. Rev. D* **105** (2022) 102004 [2102.08764].
- [43] A.O. Sushkov, *Quantum Science and the Search for Axion Dark Matter*, *PRX Quantum* **4** (2023) 020101 [2304.11797].
- [44] A.V. Dixit, S. Chakram, K. He, A. Agrawal, R.K. Naik, D.I. Schuster et al., *Searching for Dark Matter with a Superconducting Qubit*, *Phys. Rev. Lett.* **126** (2021) 141302 [2008.12231].
- [45] H. Shi and Q. Zhuang, *Ultimate precision limit of noise sensing and dark matter search*, *npj Quantum Inf.* **9** (2023) 27 [2208.13712].
- [46] S.K. Lamoreaux, K.A. van Bibber, K.W. Lehnert and G. Carosi, *Analysis of single-photon and linear amplifier detectors for microwave cavity dark matter axion searches*, *Phys. Rev. D* **88** (2013) 035020 [1306.3591].
- [47] J. Bardeen, L.N. Cooper and J.R. Schrieffer, *Theory of superconductivity*, *Phys. Rev.* **108** (1957) 1175.
- [48] P.W. Anderson and P. Morel, *Generalized bardeen-cooper-schrieffer states and the proposed low-temperature phase of liquid he^3* , *Phys. Rev.* **123** (1961) 1911.
- [49] R. Balian and N.R. Werthamer, *Superconductivity with pairs in a relative p wave*, *Phys. Rev.* **131** (1963) 1553.
- [50] A.J. Leggett, *Theory of a superfluid fermi liquid. i. general formalism and static properties*, *Phys. Rev.* **140** (1965) A1869.
- [51] A.J. Leggett, *Spin susceptibility of a superfluid fermi liquid*, *Phys. Rev. Lett.* **14** (1965) 536.
- [52] D.D. Osheroff, W.J. Gully, R.C. Richardson and D.M. Lee, *New magnetic phenomena in liquid he^3 below 3 mk*, *Phys. Rev. Lett.* **29** (1972) 920.
- [53] D. Vollhardt, P. Wölfle and R.B. Hallock, *The Superfluid Phases of Helium 3*, Taylor & Francis, London (1990).
- [54] W.F. Brinkman and P.W. Anderson, *Anisotropic superfluidity in 3He : Consequences of the spin-fluctuation model*, *Phys. Rev. A* **8** (1973) 2732.
- [55] N.D. Mermin and C. Stare, *Ginzburg-landau approach to $l \neq 0$ pairing*, *Phys. Rev. Lett.* **30** (1973) 1135.
- [56] H. Choi, J. Davis, J. Pollanen, T. Haard and W. Halperin, *Strong coupling corrections to the ginzburg-landau theory of superfluid he^3* , *Physical Review B* **75** (2007) 174503.
- [57] Y. Kawaguchi and M. Ueda, *Spinor bose-einstein condensates*, *Physics Reports* **520** (2012) 253.

- [58] D.M. Stamper-Kurn and M. Ueda, *Spinor Bose gases: Symmetries, magnetism, and quantum dynamics*, *Rev. Mod. Phys.* **85** (2013) 1191.
- [59] H. Godfrin and E. Krotscheck, *The dynamics of quantum fluids*, *arXiv preprint arXiv:2206.06039* (2022) .
- [60] M.A. Lee, K.E. Schmidt, M.H. Kalos and G.V. Chester, *Green's function monte carlo method for liquid ^3He* , *Phys. Rev. Lett.* **46** (1981) 728.
- [61] R.M. Panoff and J. Carlson, *Fermion monte carlo algorithms and liquid ^3He* , *Phys. Rev. Lett.* **62** (1989) 1130.
- [62] V.R. Pandharipande and R.B. Wiringa, *Variations on a theme of nuclear matter*, *Rev. Mod. Phys.* **51** (1979) 821.
- [63] E. Manousakis, S. Fantoni, V.R. Pandharipande and Q.N. Usmani, *Microscopic calculations for normal and polarized liquid ^3He* , *Phys. Rev. B* **28** (1983) 3770.
- [64] A. Schneider et al., *Direct measurement of the $^3\text{He}^+$ magnetic moments*, *Nature* **606** (2022) 878 [2206.05943].
- [65] H. Watanabe and H. Murayama, *Unified Description of Nambu-Goldstone Bosons without Lorentz Invariance*, *Phys. Rev. Lett.* **108** (2012) 251602 [1203.0609].
- [66] Y. Hidaka, *Counting rule for Nambu-Goldstone modes in nonrelativistic systems*, *Phys. Rev. Lett.* **110** (2013) 091601 [1203.1494].
- [67] D.S. Greywall, *^3He specific heat and thermometry at millikelvin temperatures*, *Phys. Rev. B* **33** (1986) 7520.
- [68] M. Gorghetto and G. Villadoro, *Topological Susceptibility and QCD Axion Mass: QED and NNLO corrections*, *JHEP* **03** (2019) 033 [1812.01008].
- [69] L.F. Abbott and P. Sikivie, *A Cosmological Bound on the Invisible Axion*, *Phys. Lett. B* **120** (1983) 133.
- [70] M. Dine and W. Fischler, *The Not So Harmless Axion*, *Phys. Lett. B* **120** (1983) 137.
- [71] P.D. Group, R. Workman, V. Burkert, V. Crede, E. Klempt, U. Thoma et al., *Review of particle physics*, *Progress of theoretical and experimental physics* **2022** (2022) 083C01.
- [72] S. Chigusa, T. Moroi and K. Nakayama, *Detecting light boson dark matter through conversion into a magnon*, *Phys. Rev. D* **101** (2020) 096013 [2001.10666].
- [73] D. Einzel, *Spin dependent transport and relaxation parameters of ^3He -b*, *Physica B+C* **108** (1981) 1143.
- [74] X. Zhang, C.-L. Zou, L. Jiang and H.X. Tang, *Strongly coupled magnons and cavity microwave photons*, *Phys. Rev. Lett.* **113** (2014) 156401.
- [75] Y. Tabuchi, S. Ishino, T. Ishikawa, R. Yamazaki, K. Usami and Y. Nakamura, *Hybridizing ferromagnetic magnons and microwave photons in the quantum limit*, *Physical review letters* **113** (2014) 083603.
- [76] Y. Tabuchi, S. Ishino, A. Noguchi, T. Ishikawa, R. Yamazaki, K. Usami et al., *Quantum magnonics: The magnon meets the superconducting qubit*, *Comptes Rendus Physique* **17** (2016) 729.
- [77] K. van Bibber, K. Lehnert and A. Chou, *Putting the squeeze on the axion*, *Physics today* (2020) .

- [78] A.A. Clerk, M.H. Devoret, S.M. Girvin, F. Marquardt and R.J. Schoelkopf, *Introduction to quantum noise, measurement, and amplification*, *Rev. Mod. Phys.* **82** (2010) 1155.
- [79] Y.K. Semertzidis et al., *Axion Dark Matter Research with IBS/CAPP*, [1910.11591](#).
- [80] M.D. Bird, *Ultra-high field solenoids and axion detection*, in *Microwave Cavities and Detectors for Axion Research*, G. Carosi and G. Rybka, eds., (Cham), pp. 9–16, Springer International Publishing, 2020.
- [81] J. Lough et al., *First Demonstration of 6 dB Quantum Noise Reduction in a Kilometer Scale Gravitational Wave Observatory*, *Phys. Rev. Lett.* **126** (2021) 041102 [[2005.10292](#)].
- [82] R. Dassonneville, R. Assouly, T. Peronmin, A.A. Clerk, A. Bienfait and B. Huard, *Dissipative Stabilization of Squeezing Beyond 3 dB in a Microwave Mode*, *PRX Quantum* **2** (2021) 020323 [[2102.02863](#)].
- [83] T. Kashiwazaki, T. Yamashima, K. Enbutsu, T. Kazama, A. Inoue, K. Fukui et al., *Over-8-dB squeezed light generation by a broadband waveguide optical parametric amplifier toward fault-tolerant ultra-fast quantum computers*, [2301.12658](#).
- [84] H. Vahlbruch, M. Mehmet, K. Danzmann and R. Schnabel, *Detection of 15 db squeezed states of light and their application for the absolute calibration of photoelectric quantum efficiency*, *Phys. Rev. Lett.* **117** (2016) 110801.
- [85] P. Carenza, T. Fischer, M. Giannotti, G. Guo, G. Martínez-Pinedo and A. Mirizzi, *Improved axion emissivity from a supernova via nucleon-nucleon bremsstrahlung*, *JCAP* **10** (2019) 016 [[1906.11844](#)].
- [86] M.V. Beznogov, E. Rrapaj, D. Page and S. Reddy, *Constraints on Axion-like Particles and Nucleon Pairing in Dense Matter from the Hot Neutron Star in HESS J1731-347*, *Phys. Rev. C* **98** (2018) 035802 [[1806.07991](#)].
- [87] C. O'HARE, *cajohare/axionlimits: Axionlimits*, July, 2020. [10.5281/zenodo.3932430](#).
- [88] M. Martinello, D. Bice, C. Boffo, S. Chandrasekeran, G. Ereameev, F. Furuta et al., *Q-factor optimization for high-beta 650 mhz cavities for pip-ii*, *Journal of Applied Physics* **130** (2021) .
- [89] T. Kashiwazaki, T. Yamashima, N. Takanashi, A. Inoue, T. Umeki and A. Furusawa, *Fabrication of low-loss quasi-single-mode PPLN waveguide and its application to a modularized broadband high-level squeezer*, *Appl. Phys. Lett.* **119** (2021) 251104 [[2201.01457](#)].
- [90] J.W. Foster, N.L. Rodd and B.R. Safdi, *Revealing the Dark Matter Halo with Axion Direct Detection*, *Phys. Rev. D* **97** (2018) 123006 [[1711.10489](#)].